Design considerations and workspace computation of 2-X and 2-R planar cable-driven tensegrity-inspired manipulators

Vimalesh Muralidharan, Philippe Wenger, Christine Chevallereau

To cite this version:

Vimalesh Muralidharan, Philippe Wenger, Christine Chevallereau. Design considerations and workspace computation of 2-X and 2-R planar cable-driven tensegrity-inspired manipulators. Mechanism and Machine Theory, 2024, 195, pp.105610. 10.1016/j.mechmachtheory.2024.105610 . hal-04507710

HAL Id: hal-04507710
https://hal.science/hal-04507710v1

Submitted on 17 Mar 2024

Design considerations and workspace computation of 2-X and 2-R planar cable-driven tensegrity-inspired manipulators

Vimalesh Muralidharan[a,*], Philippe Wenger[a], Christine Chevallereau[a]

[a] *Nantes Université, Ecole Centrale de Nantes, CNRS, LS2N, 44321 Nantes, France*

Abstract

This study considers two-degree-of-freedom planar tensegrity-inspired manipulators composed of anti-parallelogram (X) and revolute (R) joints containing springs and actuated remotely by four cables. The goal is to design the constituent elements of these manipulators while they carry a given payload in the presence of gravity. While this is a classical problem in serial and parallel manipulators with known approaches in the literature, their extension to tensegrity-inspired manipulators is challenging due to the presence of springs and actuation by cables. In this paper, we address all these challenges in a sequence for the 2-X and 2-R manipulators. Firstly, we discuss the limits on joint movement due to the geometry and spring free length. Then, we find the set of all feasible springs that can be installed on these joints while respecting their mechanical constraints, e.g., maximum elongation. We estimate the axial loads in the bars to obtain cross-sections safe from buckling failure. Finally, we compute the stable wrench-feasible joint space (SWFJ) and stable wrench-feasible workspace (SWFW) for the two manipulators. The ultimate objective of this study is design optimization of these manipulators.

Keywords: Tensegrity-inspired manipulators, Antagonistic actuation, Feasible springs, Safe bar sections, Stable wrench-feasible workspace

Nomenclature

DoF	Degree-of-freedom
R	Revolute joint
X	Anti-parallelogram joint
l, b	Lengths of bars in the X-joint
r, h	Semi-base length, height of isosceles triangles in R-joint
α_i	Orientation of the top bar of the i^{th} joint w.r.t. its base
$\overline{\overline{\alpha_{\max}}}$	Upper bound for α_i due to geometry of the joint and cable actuation
σ_α	Fraction $\in \,]0, 1[$ used to set safe joint limits
$\overline{\alpha_{\max}}$	$(< \overline{\overline{\alpha_{\max}}})$ safe upper bound for α_i inside the limits due to geometry and actuation
$k_i, l_{0_i}, l_{\max_i}$	Stiffness, free length, maximum operating length of springs installed in i^{th} joint
$\alpha_{\max_i}$	$(\leq \overline{\alpha_{\max}})$ actual upper bound for α_i considering the spring free length (l_{0_i})
d, D, N_a	Wire diameter, coil diameter, number of active coils of a spring
l_{b_j}, r_{b_j}, m_j	Length, cross-section radius, mass of the j^{th} bar in the manipulator
F_{l_i}, F_{r_i}	Forces imposed by the left, right cables on the i^{th} joint
$F_{\min}, F_{\max}$	Minimum, maximum bounds on the cable forces
$m_{\text{p}}, F_{\text{p}}$	Mass, weight of the point mass payload at end-effector
SWFJ	Stable wrench-feasible joint space (α_1, α_2) of a manipulator
SWFW	Stable wrench-feasible workspace (x, y) of a manipulator

---

[*] Corresponding author, Phone: +33 (0)240376919.

Email addresses: `m.vimalesh94@gmal.com` (Vimalesh Muralidharan), `Philippe.Wenger@ls2n.fr` (Philippe Wenger), `Christine.Chevallereau@ls2n.fr` (Christine Chevallereau)

1. Introduction

Recently, there has been a growing interest in developing manipulators for safe interactions with the environment and collaboration with humans [1],[2]. In this regard, nature has been a great source of inspiration for roboticists to develop robots with such enhanced capabilities [3]. In the literature, one finds several bio-inspired systems for soft interactions [4],[5]. These are inspired mainly by flexible organs of continuous-bodied organisms (e.g., tentacles of octopus [6]) or the musculoskeletal system of vertebrate animals (e.g., arm of human [7]).

A lot of research has been devoted to bio-inspired continuous-bodied robots, commonly called continuum robots [8]. Their thin form and adaptability to unstructured environments make them ideally suited for surgical applications, e.g., [9]. These robots are driven extrinsically by cables/tubes/rods or intrinsically by pressurized fluids, depending on the environmental constraints [10].

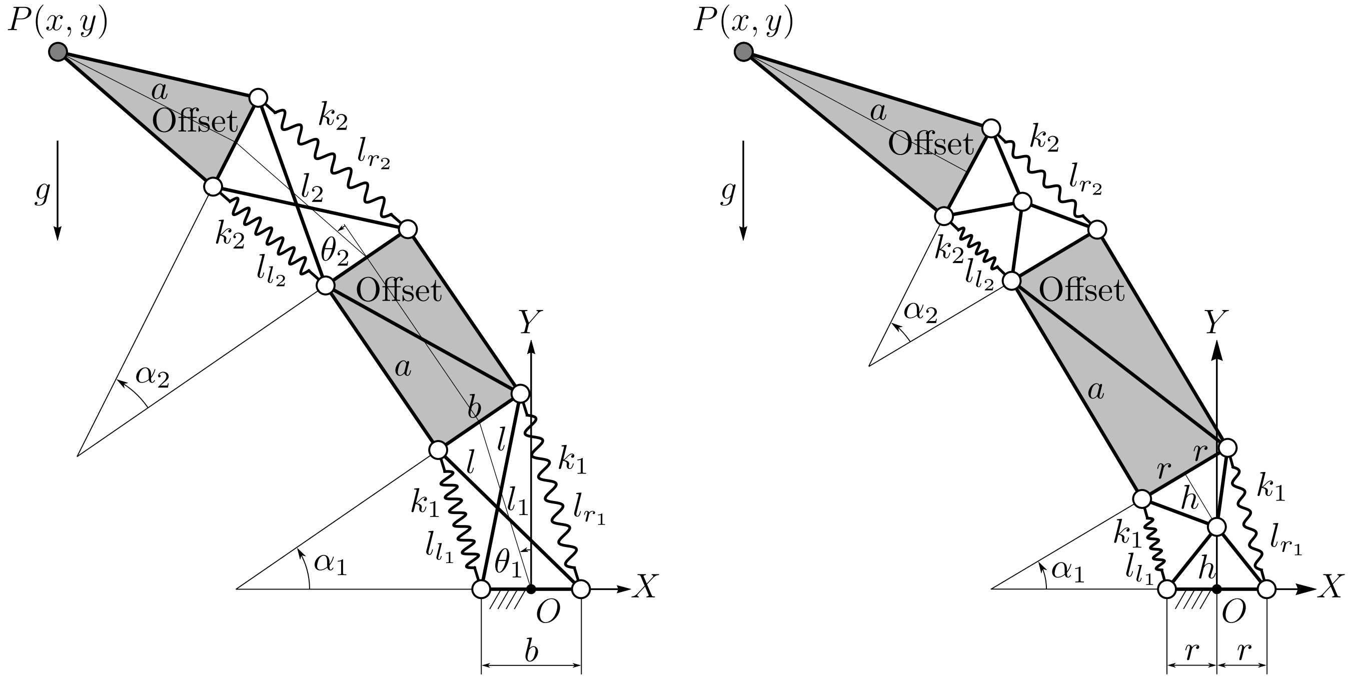

(a) 2-X manipulator

(b) 2-R manipulator

Figure 1: Schematics of the manipulators under study: 2-X (left) and 2-R (right).

In contrast, a musculoskeletal system consists of joints formed by contact between surfaces of bones, supported by ligaments, and actuated by muscles. In a bio-inspired robotic system, these elements are substituted with bars, springs, and cables for practical realization [11]. These elements are also typically found in tensegrity systems [12]. Drawing inspiration from them, two manipulators based on the musculoskeletal/tensegrity paradigm, shown in Fig. 1, are studied in this paper. However, the form of these manipulators differs from the authentic tensegrity systems (see, e.g., [13]) in a few ways, as explained in the following.

The concept of tensegrity originated in architecture, with the emergence of artistic structures containing "floating" rigid bodies held together by cables. On the contrary, tensegrity-inspired manipulators are systems designed to exhibit controlled motions through actuation with motors. They also contain mechanical connections (joints) between the rigid bodies to limit their degree-of-freedom (DoF) to less than six, as required by the application, see, e.g., other planar tensegrity mechanisms [14],[15]. Another point of difference is that in conventional tensegrity structures, only cables/springs support tensile loads and not rigid bodies. However, in the tensegrity-inspired manipulators, the loading pattern changes with their movement, and consequently, some bars experience tensile loading in some configurations.

Despite these differences, the feasible configurations of the tensegrity-inspired manipulators are determined by the conditions of static equilibrium and stability, as in the case of conventional tensegrity structures. Hence, it is justified to refer to them as tensegrity-inspired manipulators.

Another challenge in tensegrity-inspired manipulators is to choose an appropriate actuation scheme. Since there are several possibilities for actuation, selecting a good actuation scheme is not an intuitive one [16]. In this regard, antagonistic actuation of cables is a scheme that preserves the ability to prestress the mechanism [17]. In most tensegrity mechanisms, the actuator(s) are used to control the position of some nodes (attachment points between components) by implicitly using a closed-loop control scheme (with sensor feedback). However, there are a few others where the actuators are used only to impose the tension in cables with an open-loop control scheme (without sensor feedback) [18],[19]. This study will assume the latter scheme owing to its simplicity.

The objective of this work is to present the various factors to consider while designing tensegrity-inspired manipulators for carrying a payload, similar to those of serial and parallel manipulators [20],[21], and eventually perform their design optimization. Firstly, the design of tensegrity-inspired manipulators must also consider the springs, whose mechanical feasibility conditions are more challenging to incorporate inside the overall design of the manipulator. Secondly, the cross-sections of the bars must also be chosen appropriately based on the payload weight, forces due to springs, and cable routing to prevent buckling failure. Finally, unlike in a conventional manipulator, the workspace of the tensegrity-inspired manipulators is not only determined by kinematic factors such as singularities and joint limits but is further qualified by the conditions of static equilibrium and stability, which makes its computation more involved [22].

This paper addresses the above design challenges for two planar tensegrity-inspired manipulators shown in Fig. 1. The significant contributions of this work may be summarized as follows:

- All the conditions of mechanical feasibility for the springs (with non-zero free lengths) are considered to derive the total feasible design space for them. A two-parameter representation of this space is presented to access all the springs.
- The limits of movement for each of the joints in the manipulator are studied systematically by considering their geometry, actuation scheme of cables, and free length of springs installed in them.
- A geometric method is proposed to estimate the axial forces in the bars conservatively within the permissible range of movement. This estimation is used to design sufficiently large cross-sections to avoid bucking failure.
- The steps involved in the computation of the stable wrench-feasible workspace (SWFW) are illustrated for the 2-X and 2-R tensegrity-inspired manipulators.

The rest of this paper is organized as follows: the architectures of the two manipulators are described in Section 2. The design considerations and steps involved in the computation of SWFW are discussed for the 2-X and 2-R manipulators in Sections 3 and 4, respectively. Finally, the conclusions of this study are presented in Section 5.

2. Description of the two tensegrity-inspired manipulators

The schematics of two planar positioning manipulators, namely 2-X and 2-R, are shown in Figs. 1(a) (left) and 1(b) (right), respectively. They are each a two-degree-of-freedom (2-DoF) robotic system used to control the position of an end-effector point $P(x, y)$, containing a point payload of mass m_p.

The 2-X manipulator comprises two anti-parallelogram (X) joints arranged in series with rigid offsets (highlighted in shading) as shown in Fig. 1(a). Each X-joint consists of a top bar and a base bar of length b, and two crossed bars of length l, satisfying the condition $(l > b)$ for its assembly. All the bars are connected to their neighbors with pivots.

On the other hand, the 2-R manipulator has R-joints instead of X-joints, with the same arrangement of offsets, as illustrated in Fig. 1(b). An R-joint contains two congruent isosceles triangles (each composed of three bars), one inverted on top of the other. The semi-base length r and height h specify the geometry of these triangles.

In both manipulators, for joint i, the orientation of the top bar relative to its base is denoted by α_i, with $i = 1, 2$, as shown in Fig. 1. The joint i is equipped with two identical extension springs of stiffness k_i and free length l_{0_i}, on either side to ensure that the manipulator remains in stable equilibrium at the home configuration $(\alpha_1, \alpha_2) = (0, 0)$ rad[1] when no external forces (other than the gravitational forces) are applied. In both manipulators, there exist two rigid offsets (in the form of trusses) of length a between the two joints and between the second joint and the end-effector point P, as indicated by the shaded portions in Fig. 1. Note that the purpose of shading is only to differentiate between the offsets and joints, while both are composed of bars and pivots[2]. All the bars and springs are arranged in parallel planes to avoid any interference between them. This arrangement also provides improved rigidity for these manipulators in the direction normal to the plane of movement, as is necessary for their practical realization. All the bars are assumed to be inelastic in this study.

The manipulators are placed such that their plane of motion is parallel to the direction of gravity (see Fig. 1), unlike a conventional SCARA robot [23]. This placement ensures that the moments induced due to the weight of bars/payload are parallel to the axes of the pivots, which they cannot transmit. Since pivots connect all the elements, there is only a transmission of axial forces between them. In order to preserve this property and keep the moving structure light, these manipulators will be actuated *remotely* by motors installed on the ground, using cables as transmission elements.

The visible difference between the two architectures is that for the 2-R manipulator, the two instant centers of rotations are located at the "central" pivots of the R-joints, while for the 2-X manipulator, the centers of rotations are not at fixed pivots but at the virtual intersection of diagonal bars of the X-joints. The hidden difference is that the antagonistic cable actuation produces different effects on the stiffness of the two manipulators, as in the case of single X- and R-joints explained in [18].

---

[1] In this paper, all the angular parameters are presented in radians unless specified otherwise.

[2] In this paper, the term pivot represents the connection between two neighboring elements (bars/springs) in the manipulator, while, the term revolute joint (R-joint) represents the complete joint module inclusive of the two triangles and springs.

The following sections will discuss the design considerations for the 2-X and 2-R manipulators.

3. Design considerations for 2-X manipulator

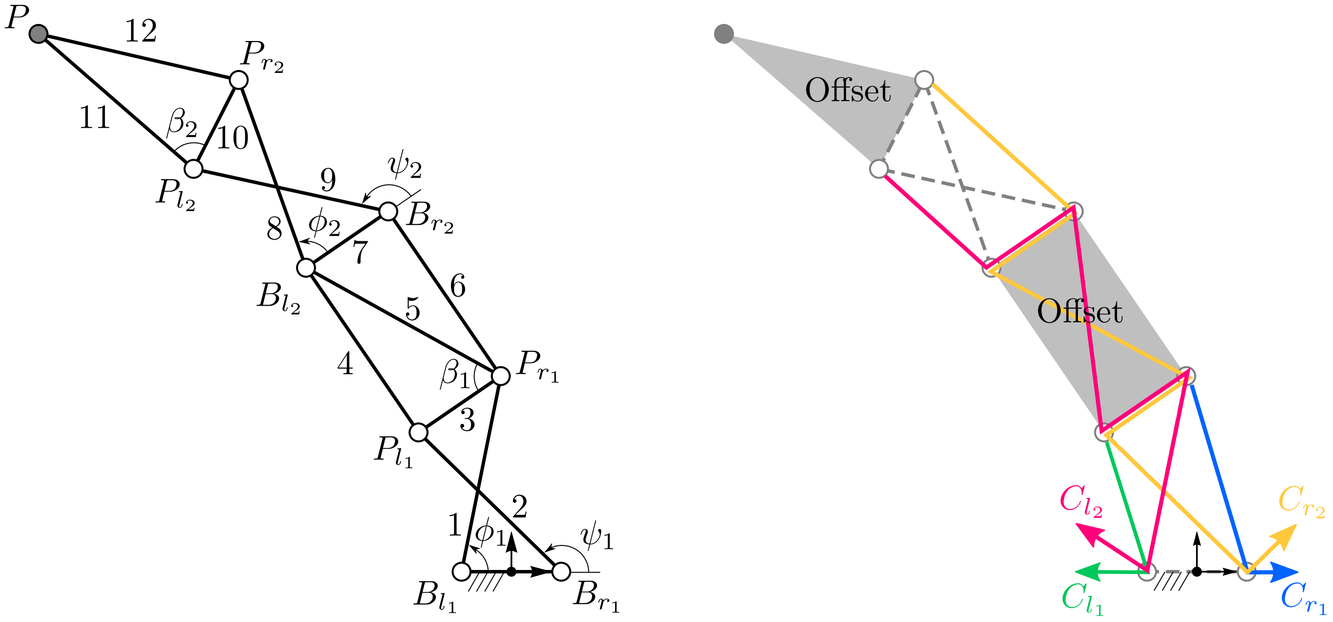

(a) Bar labels

(b) Cable routing

Figure 2: Bar labels (left) and cable routing scheme (right) for the 2-X manipulator.

A schematic showing the labels of all the moving bars and pivots of the 2-X manipulator is presented in Fig. 2(a), and will be referred to in the following sections. Four motors actuate this manipulator using one cable each, as depicted in Fig. 2(b). The cables C_{l_1} and C_{r_1} actuate the first X-joint *antagonistically*, while the cables C_{l_2} and C_{r_2} actuate the second joint in a similar manner *independently* of the first one. In order to achieve this independence, the cables C_{l_2}, C_{r_2} have been routed along the bars of the first joint and the rigid offsets with pulleys, following the *strut-routed* scheme described in [24]. They have been passed through the rigid offset multiple times in a zig-zag manner to avoid loss of contact with the pulleys. This paper assumes that the cables are massless and inextensible while the pulleys are massless points with zero radii. The forces imposed by the actuating cables are bounded by $[F_{\text{min}}, F_{\text{max}}]$, with $F_{\text{min}} = 0$ N for simplicity.

Though three cables are sufficient to actuate a 2-DoF manipulator [25], four cables have been considered in this work to extend the symmetry in the architecture of the above manipulator to its actuation scheme and eventually its workspace (more details in [26]).

The various steps involved in the feasible design and workspace computation of a 2-X manipulator are summarized in Fig. 3 and are described in detail in the following sections. As a first step, safe limits for the movement of the joints are computed from the joint geometry and cable routing scheme in Section 3.1. These limits are used to define the complete feasible design space for the springs in Section 3.2. Inside this design space, the designer must independently choose springs for each joint. Then, the actual joint limits for each joint are determined based on the free length of the springs installed in it (discussed in Section 3.1). These data, along with the user-defined maximal actuation forces and payload, are used to estimate the axial forces in the bars and define safe cross-sections for them in Section 3.3. These data are used to develop the static model of the manipulator in Section 3.4, followed by the kinematic model in Section 3.5. The steps involved in the computation of SWFW are presented in Section 3.6. Finally, the entire process is illustrated with a numerical example in Section 3.7.

3.1. Joint limits for i^{th} X-joint

The range of movement of an X-joint is limited by the flat singularities at $\alpha_i = \pm\pi$. A static analysis shows that the forces in the bars of the joint tend to infinity while it approaches these singularities (more details to follow in Section 3.3.2). Thus, it is necessary to set safe limits $[-\overline{\alpha_{\text{max}}}, \overline{\alpha_{\text{max}}}]$, such that $\overline{\alpha_{\text{max}}}(< \pi)$ for all the joints to keep them far from flat singularities.

In addition to the above limits, which apply identically to all the X-joints, the movement of the i^{th} X-joint in the serial chain could be further limited by the springs installed in it (see Fig. 4(a)). This limit arises because the extension springs cannot have a length smaller than their free length. The lengths of the springs (or, equivalently distance between their attachment points) on either side of the joint can be computed as (see [18]):

$$l_{l_i}(\alpha_i) = -b\sin(\alpha_i/2) + \sqrt{l^2 - b^2\cos^2(\alpha_i/2)} \qquad l_{r_i}(\alpha_i) = b\sin(\alpha_i/2) + \sqrt{l^2 - b^2\cos^2(\alpha_i/2)} \tag{1}$$

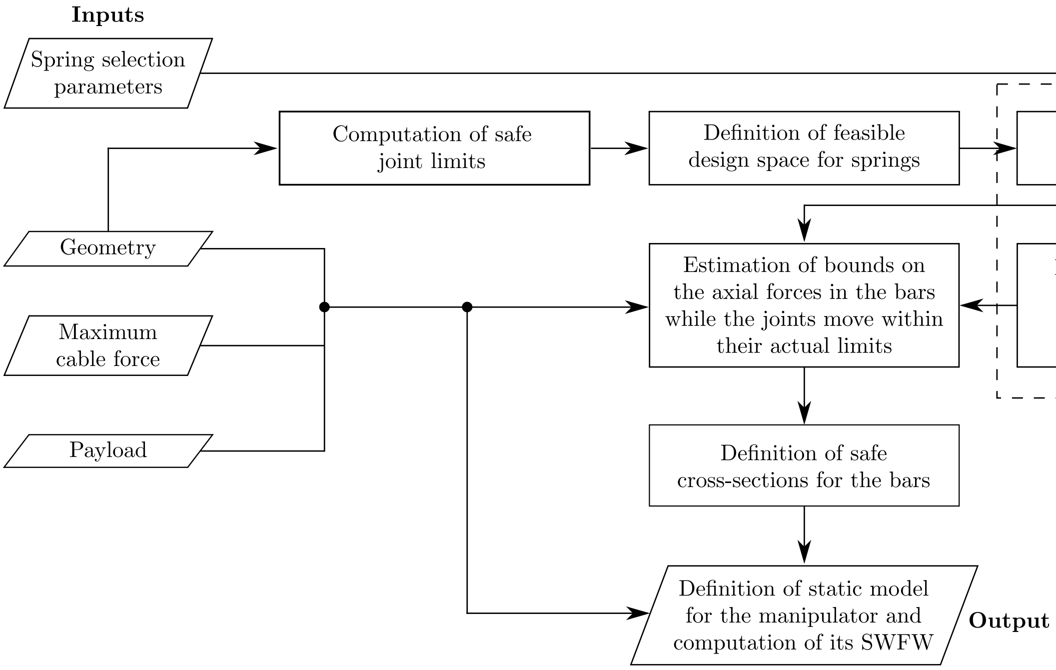

Figure 3: Sequence of treating the design considerations for the 2-X manipulator.

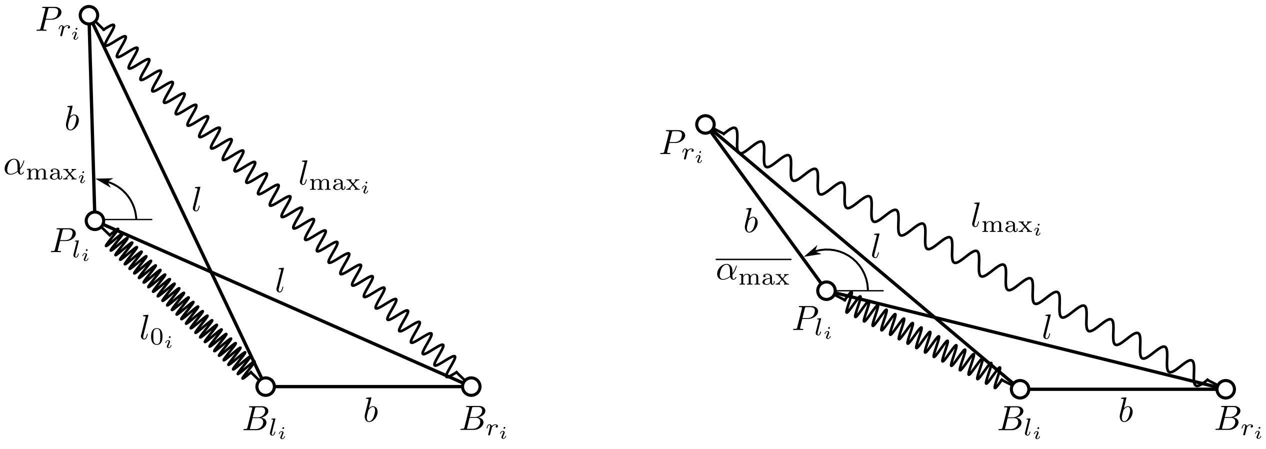

(a) Case A: $l_{l_i}\left(\overline{\alpha_{\max}}\right) < l_{0_i} < \sqrt{l^2 - b^2}$

(b) Case B: $0 < l_{0_i} \leq l_{l_i}\left(\overline{\alpha_{\max}}\right)$

Figure 4: Joint limits of an X-joint depending on the spring free length and bar lengths.

Since we use identical springs on the two sides, it is apparent that their free length must be in the range $\left]0, \sqrt{l^2-b^2}\right[$ for their installation. Further study of joint limits bifurcates into two cases depending on the free length (l_{0_i}) of the springs, as follows:

- **Case A** $\left[l_{l_i}(\overline{\alpha_{\max}}) < l_{0_i} < \sqrt{l^2-b^2} \text{ in Fig. } 4(a)\right]$: In this case, the free length (l_{0_i}) of the springs in i^{th} joint happens to be more than the distance between the attachment points (P_{l_i}, B_{l_i}) at $\alpha_i = \overline{\alpha_{\max}}$. Thus, the actual amplitude of movement for i^{th} X-joint, denoted by $\alpha_{\max_i}(< \overline{\alpha_{\max}})$, will be attained when the left spring reaches its free length. Owing to the symmetry of this joint, the right spring reaches its maximum operating length $(l_{\max_i})$ at this configuration. Thus, from the geometry of the X-joint in Fig. 4(a), $\alpha_{\max_i}$ and $l_{\max_i}$ can be computed in terms of the free length (l_{0_i}) as follows:

$$\begin{cases} \alpha_{\max_i} = 2\arcsin\left(\frac{l^2-b^2-l_{0_i}^2}{2bl_{0_i}}\right) \\ l_{\max_i} = \frac{l^2-b^2}{l_{0_i}} \end{cases} \tag{2}$$

- **Case B** $[0 < l_{0_i} \leq l_{l_i}(\overline{\alpha_{\max}}) \text{ in Fig. } 4(b)]$: In this case, the free length of the springs allows the joint to reach its safe limits $\pm\overline{\alpha_{\max}}$. The maximum operating length of the springs is given by the distance between the attachment points of the spring on the right side at $\overline{\alpha_{\max}}$ (see Fig. 4(b)) as:

$$\begin{cases} \alpha_{\max_i} = \overline{\alpha_{\max}} \\ l_{\max_i} = l_{r_i}(\overline{\alpha_{\max}}) \end{cases} \tag{3}$$

In summary, from Eqs. (2),(3), it is observed that the joint limits for the i^{th} X-joint depend on the geometry (b, l), designer-specified safe limit $(\overline{\alpha_{\max}})$, and the free length (l_{0_i}) of the springs. Though the designer can choose the values of $(b, l, \overline{\alpha_{\max}})$ rather arbitrarily, the choice of free length is not an obvious one. This is because the springs with stiffness required to stabilize the manipulator may not possess the chosen free length and vice versa. Hence, a more reasonable approach would be to find all the feasible springs that can be installed in the joint based on the $(b, l, \overline{\alpha_{\max}})$ parameters and let the designer choose a suitable one. Once this choice is made, the actual joint limits $(\pm\alpha_{\max_i})$ can be determined from Eq. (2) or Eq. (3) depending on whether the free length of the chosen spring belongs to case A or case B.

In order to compute all the feasible springs, the conditions on free length (l_{0_i}) and required operating length $(l_{\max_i})$ derived in cases A and B must be used along with other feasibility conditions for the springs. This process is carried out in the next section.

3.2. Design space for the springs of i^{th} X-joint

In this section, a method to compute the complete feasible design space for the springs for an X-joint with known geometry (b, l) and safe joint limits $(\pm\overline{\alpha_{\max}})$ is presented briefly. More details can be found in the associated technical report [27].

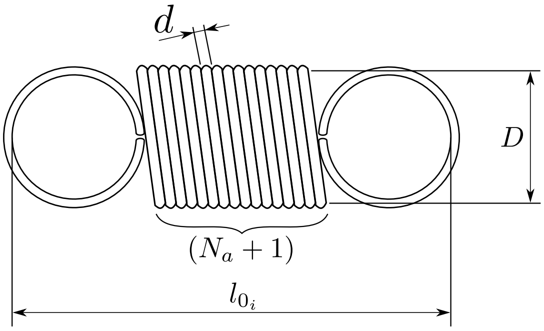

Figure 5: Schematic of a helical extension spring.

The schematic of a helical extension spring with stiffness k_i and free length l_{0_i} is shown in Fig. 5. It is fabricated by winding a steel wire of diameter d around a cylinder successively to form identical coils of nominal diameter D. The number of active coils, N_a, which contribute to the elongation of the spring is conventionally assumed to be one less than the total number of coils in the body (see, e.g., [28], p. 357). The initial tension in the spring is neglected in this study [27].

One commonly used material for manufacturing springs is EN 10720-1 (SH/DH) (equivalently ASTM A228), also known as music/piano wire. This material will be assumed for all the springs uniformly in this paper. From the standard [29], one finds the shear modulus (G_k) as 81.5 GPa and volumetric density (ρ_k) as 7850 kg/m^3.

Using Fig. 5, the mass of the spring inclusive of the two hooks can be computed as:

$$m_{k_i} = \frac{1}{4}\rho_k(\pi d)^2 D(N_a+3) \tag{4}$$

While the material is known, the spring parameters $\{k_i, d, D, N_a, l_{0_i}\}$ can completely define a spring. However, they must also respect two equations. The first one is the relation between the spring stiffness and its geometry and material properties (see [28], p. 355), while the second one is the geometric relation between the free length and other parameters (see Fig. 5):

$$k_i = \frac{G_k d^4}{8N_a D^3} \implies N_a = \frac{G_k d^4}{8k_i D^3} \tag{5}$$

$$l_{0_i} = (N_a + 1)d + 2(D - d) \tag{6}$$

Thus, only three of the above parameters can be chosen independently to define a spring. In this paper, (k, d, D) are treated as independent parameters while (N_a, l_{0_i}) are determined from Eqs. (5) and (6), respectively.

In addition, there are several inequality conditions that must be respected by the spring (see [27] for more details):

$$\begin{cases} \chi_1 : \text{coils must be strong enough to support the specified deflection} \\ \chi_2 : \text{there should be more than three active coils} \\ \chi_3 : \text{the spring index } (D/d) \text{ must be bounded inside } [4, 20] \\ \chi_4 : \text{the helix angle must be less than } 7.5^\circ \end{cases} \tag{7}$$

Note that the conditions χ_1, χ_4 depend on the desired maximum elongation $(l_{\max_i})$ of the spring [27]. Furthermore, for incorporating the spring into X-joint, the following conditions must be considered:

$$\begin{cases} \chi_5 : \text{the outer diameter } (D + d) \text{ must be less than one third the joint width } (b/3) \text{ for compactness} \\ \chi_6 : \text{condition on } l_{0_i} \text{ in case A (denoted } \chi_{6a}) \text{ or case B (denoted } \chi_{6b}) \text{ as in Section 3.1} \end{cases} \tag{8}$$

Recalling that the conditions on l_{0_i} and the respective expressions of $l_{\max_i}$ are different in cases A and B discussed above, we come up with two sets of feasibility conditions for the springs. The ones corresponding to case A are consolidated into $\boldsymbol{\chi}_a$ and those corresponding to case B in $\boldsymbol{\chi}_b$, as follows:

$$\boldsymbol{\chi}_a = \begin{cases} \chi_1 \left(l_{\max_i} = \frac{l^2 - b^2}{l_{0_i}}\right) \\ \chi_2 \\ \chi_3 \\ \chi_4 \left(l_{\max_i} = \frac{l^2 - b^2}{l_{0_i}}\right) \\ \chi_5 \\ \chi_{6a} := l_{0_i} \in \left]l_{l_i}(\overline{\alpha_{\max}}), \sqrt{l^2 - b^2}\right[\end{cases} \qquad \boldsymbol{\chi}_b = \begin{cases} \chi_1 \left(l_{\max_i} = l_{r_i}(\overline{\alpha_{\max}})\right) \\ \chi_2 \\ \chi_3 \\ \chi_4 \left(l_{\max_i} = l_{r_i}(\overline{\alpha_{\max}})\right) \\ \chi_5 \\ \chi_{6b} := l_{0_i} \in \left]0, l_{l_i}(\overline{\alpha_{\max}})\right] \end{cases} \tag{9}$$

The above conditions can be formulated solely in terms of the independent spring parameters (k, d, D) using Eqs. (5),(6), as illustrated in [27]. The set of all (k, d, D) values satisfying $\boldsymbol{\chi}_a$ (resp. $\boldsymbol{\chi}_b$) form the feasible design space for springs belonging to case A (resp. B). The complete feasible design space for the springs is obtained from the union of the two sets $\boldsymbol{\chi}_a \cup \boldsymbol{\chi}_b$.

It is customary to use only standard values for the wire diameter (d) for its accurate fabrication, as it is the most influential parameter in the spring design (see Eqs. (5),(6)). Thus, in this study, the wire diameter is assumed to be a discrete variable that takes the following values $d = \{0.2, 0.3, \ldots, 6\}$ mm.

As a numerical illustration, consider the X-joint with geometry: $b = 0.2$ m, $l = 0.4$ m, and safe joint limit $\overline{\alpha_{\max}} = 5\pi/6$ rad. A slice of the spring space for $k_i = 3000$ N/m is shown in Fig. 6(a). The vertical grid lines represent the chosen discrete values of d. For each value of d, D can vary inside an interval Δ_j to generate feasible spring designs. These feasible intervals on each grid line are shown in blue. In this example, all the feasible springs belong to set $\boldsymbol{\chi}_a$.

There are a total of 37 feasible intervals $\Delta_1, \Delta_2, \ldots, \Delta_{37}$ of D for different values of d, as shown in Fig. 6(a). These intervals can be normalized w.r.t. the sum of all the interval sizes $\sum_{j=1}^{37} \Delta_j$, to form $\Delta_j^{'}$. This permits one to arrange them successively as in Fig. 6(b), to create a *bijective* map between the feasible intervals and a fraction $\sigma_{k_i} \in [0, 1]$. For instance, when $\sigma_{k_i} = 1.0$, the corresponding point in the feasible space is found to be $(d, D) = (6.0, 58.4844)$ mm, as depicted in Fig. 6(b). In this manner, all the feasible points in (d, D) space can be accessed with just a single parameter σ_{k_i}.

It is noted that the map from σ_{k_i} to the intervals has several discontinuities as observed from Fig. 6(b). At all such values of σ_{k_i}, the right-sided limit for $d(\sigma_{k_i})$ has been assigned arbitrarily. This leads to the loss of the upper bounding point in all the intervals, except the last one. However, the loss of a few discrete points in an ∞^1 space is an acceptable compromise to obtain a one-parameter (σ_{k_i}) representation of that space.

In summary, the complete feasible design space for the springs of an X-joint i, with known geometry (l, b) and safe joint limits $(\pm\overline{\alpha_{\max}})$, can be described with just two parameters (k_i, σ_{k_i}) with $\sigma_{k_i} \in [0, 1]$. The wire and coil diameters (d, D) of the springs can be found from the mapping illustrated in Fig. 6(b). The remaining parameters, namely, number of active coils, free length, and mass, can be found using Eqs. (5),(6),(4), respectively. In the above example, when $k_i = 3000$ N/m, $\sigma_{k_i} = 1.0$, $(d, D) = (6.0, 58.4844)$ mm, the other parameters are found to be: $N_a = 22.0005$, $l_{0_i} = 0.2430$ m, $m_{k_i} = 1.0195$ kg. Further,

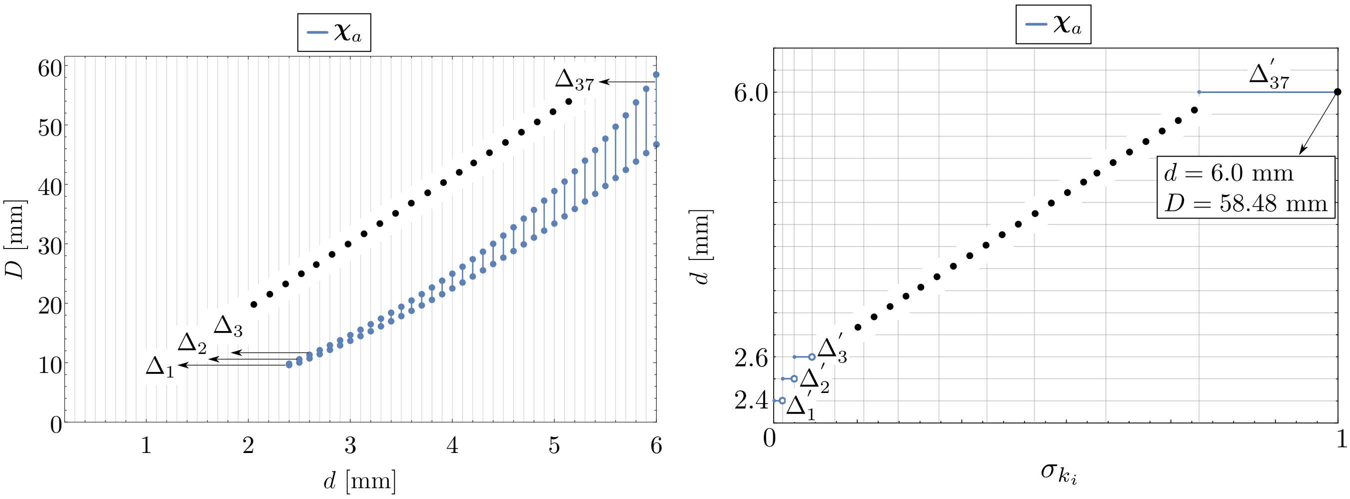

(a) Feasible intervals Δ_j of D in (d, D) space

(b) Normalization of Δ_j w.r.t. $\Sigma_j \Delta_j$ and its successive arrangement forming a map to $\sigma_{k_i} \in [0, 1]$

Figure 6: Parametrization of the feasible spring space with $\sigma_{k_i} \in [0, 1]$ when $k_i = 3000$ N/m for an X-joint with $b = 0.2$ m and $l = 0.4$ m, and $\overline{\alpha_{\max}} = 5\pi/6$ rad.

from Eq. (2), the actual upper limit of movement for this joint is computed to be $\alpha_{\max_i} = 1.3561$ rad and the maximum operating length of this spring is $l_{\max_1} = 0.4939$ m.

In the next section, the data of springs and actual limits for all the joints will be used to estimate the forces in the bars and design safe cross-sections for them.

3.3. *Cross-sections and masses of the bars of 2-X manipulator*

This section presents a method to determine safe cross-sections for the bars of the 2-X manipulator, whose bar lengths, springs, maximum cable forces, and payload mass are known.

3.3.1. *Cross-section of a bar for a given buckling load*

Since it is known that the bars experience only axial loads (see Section 2), they are most likely to fail in buckling. In this study, all the bars are assumed to be made of Aluminum with a uniform circular cross-section. Let l_{b_j} and r_{b_j} denote the length and cross-section radius of the j^{th} bar, respectively, with $j = 1, \ldots, 12$ (see Fig. 2(a)). From [30], p. 819, the critical buckling load of this bar is found to be:

$$F_{\text{critical}} = \frac{\pi^2 E I_{b_j}}{l_{b_j}^2} \tag{10}$$

where $E = 70$ GPa is the Young's modulus of Aluminum, $I_{b_j} = \frac{\pi r_{b_j}^4}{4}$ is the second moment of area of the bar about an axis lying in the cross-section. Substituting for I_{b_j} and rearranging the above equation, one obtains:

$$r_{b_j} = \left(\frac{4 F_{\text{critical}} l_{b_j}^2}{E \pi^3} \right)^{1/4} \tag{11}$$

This value of r_{b_j} represents a limiting value of the cross-section radius for which the j^{th} bar will just buckle when the applied load is equal to F_{critical}. Suppose one could overestimate the load experienced by the j^{th} bar and assign it to F_{critical} in Eq. (11), a safe value for its cross-section radius can be obtained. This computation is carried out in the next section.

3.3.2. *Safe estimation for axial load in the bars*

This section aims to estimate the forces experienced by each of the bars while the manipulator is held in static equilibrium by the actuating cables. This estimation is challenging since the forces in the bars vary with the configuration and the redundant equilibrating cable forces at that configuration. Additionally, the masses of the bars and springs must also be considered for calculating these forces accurately. However, the cross-sections of the bars are not known to the designer a priori, which makes the accurate computation of the bar reactions extremely difficult. Hence, an alternate approach that provides a conservative estimation of these forces will be followed in this work.

In this approach, the masses of bars and springs are neglected since their contributions are expected to be lower than the others. Hence, the reaction forces F_j acting at the ends of each bar j must be directed along their respective longitudinal axes in

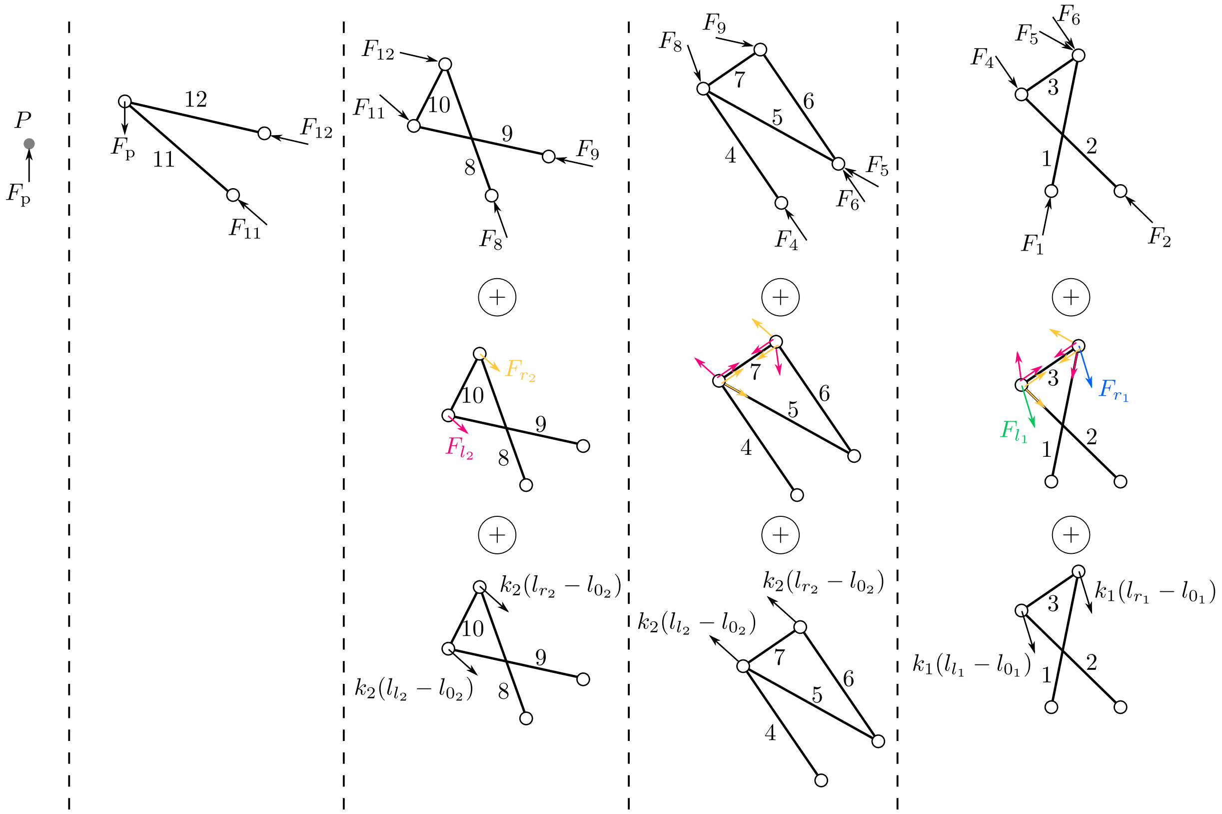

Figure 7: Reaction forces at the ends of the bars.

opposite directions. As a convention, while the forces are compressive (i.e., directed towards the geometric center), they are considered positive. While they are tensile, they are considered negative. Some of these forces and their transmissions between the bars are visualized by splitting the manipulator into many parts, as shown in the first row of Fig. 7. In addition to these, forces imposed by the cables (based on the routing shown in Fig. 2(b)) and the stiffness of springs are also considered at the various pivots, as shown in the second and third rows of Fig. 7, respectively.

The forces in each of the bars can be computed successively starting from the bars 12 and 11. From the second column in Fig. 7, it is apparent that forces induced in these two bars are only due to the payload weight F_{p}. Hence, the forces F_{12} and F_{11} can be computed by the vectorial resolution of this force along the directions of these bars. The resulting expressions are represented as: $F_{12} = \Omega_{\mathrm{p}}^{12} F_{\mathrm{p}}$ and $F_{11} = \Omega_{\mathrm{p}}^{11} F_{\mathrm{p}}$, where the coefficients of F_{p} are defined in Eq. (13).

Similarly, the net force at one end of all the bars are computed as in Eq. (12) and the expressions for force coefficients[3] are presented in Eq. (13). While $(-\pi < \alpha_i < \pi)$, it can be shown that $\theta_i = \alpha_i/2$ (see Fig. 1(a) and [24]). The other intermediate angles (ϕ_i, ψ_i) shown in Fig. 2(a) can be obtained in terms of α_i using the loop-closure equations of the X-joint (see [31]). Finally, the constant angles (β_1, β_2) in offsets shown in Fig. 2(a), can be obtained from the lengths of the bars.

$$\begin{cases} F_{12} &= \Omega_{\mathrm{p}}^{12} F_{\mathrm{p}} \\ F_{11} &= \Omega_{\mathrm{p}}^{11} F_{\mathrm{p}} \\ F_{10} &= \Omega_{11}^{10} F_{11} + \Omega_{Fk_{l_2}}^{10} (F_{l_2} + k_2(l_{l_2} - l_{0_2})) \\ F_9 &= \Omega_{11}^{9} F_{11} + \Omega_{Fk_{l_2}}^{9} (F_{l_2} + k_2(l_{l_2} - l_{0_2})) \\ F_8 &= \Omega_{12}^{8} F_{12} + \Omega_{Fk_{r_2}}^{8} (F_{r_2} + k_2(l_{r_2} - l_{0_2})) \\ F_7 &= \Omega_{9}^{7} F_9 + \Omega_{F_{l_2}}^{7} F_{l_2} + \Omega_{F_{r_2}}^{7} F_{r_2} + \Omega_{k_{r_2}}^{7} k_2(l_{r_2} - l_{0_2}) \\ F_6 &= \Omega_{9}^{6} F_9 + \Omega_{F_{l_2}}^{6} F_{l_2} + \Omega_{Fk_{r_2}}^{6} (F_{r_2} + k_2(l_{r_2} - l_{0_2})) \\ F_5 &= \Omega_{8}^{5} F_8 + \Omega_{7}^{5} F_7 + \Omega_{F_{l_2}}^{5} F_{l_2} + \Omega_{F_{r_2}}^{5} F_{r_2} + \Omega_{k_{l_2}}^{5} k_2(l_{l_2} - l_{0_2}) \\ F_4 &= \Omega_{8}^{4} F_8 + \Omega_{7}^{4} F_7 + \Omega_{F_{l_2}}^{4} F_{l_2} + \Omega_{F_{r_2}}^{4} F_{r_2} + \Omega_{k_{l_2}}^{4} k_2(l_{l_2} - l_{0_2}) \\ F_3 &= \Omega_{4}^{3} F_4 + \Omega_{F_{l_2}}^{3} F_{l_2} + \Omega_{F_{r_2}}^{3} F_{r_2} + \Omega_{Fk_{l_1}}^{3} (F_{l_1} + k_1(l_{l_1} - l_{0_1})) \\ F_2 &= \Omega_{4}^{2} F_4 + \Omega_{F_{l_2}}^{2} F_{l_2} + \Omega_{F_{r_2}}^{2} F_{r_2} + \Omega_{Fk_{l_1}}^{2} (F_{l_1} + k_1(l_{l_1} - l_{0_1})) \\ F_1 &= \Omega_{6}^{1} F_6 + \Omega_{5}^{1} F_5 + \Omega_{F_{l_2}}^{1} F_{l_2} + \Omega_{F_{r_2}}^{1} F_{r_2} + \Omega_{Fk_{r_1}}^{1} (F_{r_1} + k_1(l_{r_1} - l_{0_1})) \end{cases} \tag{12}$$

---

[3] Note that $\csc(\cdot) = 1/\sin(\cdot)$ and $\sec(\cdot) = 1/\cos(\cdot)$.

$$\begin{cases} \Omega_{\mathrm{p}}^{12} & = \csc(2\beta_2)\cos(\beta_2 + (\alpha_1+\alpha_2));\ \Omega_{\mathrm{p}}^{11} = \csc(2\beta_2)\cos(\beta_2 - (\alpha_1+\alpha_2)); \\ \Omega_{11}^{10} & = \csc(\psi_2-\alpha_2)\sin(\beta_2+\alpha_2-\psi_2);\ \Omega_{Fk_{l_2}}^{10} = \csc(\psi_2-\alpha_2)\cos(\theta_2-\psi_2); \\ \Omega_{11}^{9} & = \csc(\psi_2-\alpha_2)\sin(\beta_2);\ \Omega_{Fk_{l_2}}^{9} = \csc(\psi_2-\alpha_2)\cos(\theta_2); \\ \Omega_{12}^{8} & = \csc(\phi_2-\alpha_2)\sin(\beta_2);\ \Omega_{Fk_{r_2}}^{8} = \csc(\phi_2-\alpha_2)\cos(\theta_2); \\ \Omega_{9}^{7} & = \cos(\psi_2);\ \Omega_{F_{l_2}}^{7} = 1+\cos(\beta_1);\ \Omega_{F_{r_2}}^{7} = 1+\sin(\theta_2);\ \Omega_{k_{r_2}}^{7} = \sin(\theta_2); \\ \Omega_{9}^{6} & = \sin(\psi_2);\ \Omega_{F_{l_2}}^{6} = \sin(\beta_1);\ \Omega_{Fk_{r_2}}^{6} = -\cos(\theta_2); \\ \Omega_{8}^{5} & = -\sec(\beta_1)\cos(\phi_2);\ \Omega_{7}^{5} = -\sec(\beta_1);\ \Omega_{F_{l_2}}^{5} = \sec(\beta_1)(1-\sin(\theta_2)); \\ \Omega_{F_{r_2}}^{5} & = 1+\sec(\beta_1);\ \Omega_{k_{l_2}}^{5} = -\sec(\beta_1)\sin(\theta_2); \\ \Omega_{8}^{4} & = \sec(\beta_1)\sin(\beta_1+\phi_2);\ \Omega_{7}^{4} = \tan(\beta_1); \\ \Omega_{F_{l_2}}^{4} & = -\sec(\beta_1)\cos(\beta_1+\theta_2)-\tan(\beta_1); \\ \Omega_{F_{r_2}}^{4} & = -\tan(\beta_1);\ \Omega_{k_{l_2}}^{4} = -\sec(\beta_1)\cos(\beta_1+\theta_2); \\ \Omega_{4}^{3} & = \cot(\psi_1-\alpha_1);\ \Omega_{F_{l_2}}^{3} = 1+\csc(\alpha_1-\psi_1)\sin(\beta_1+\alpha_1-\psi_1); \\ \Omega_{F_{r_2}}^{3} & = 1;\ \Omega_{Fk_{l_1}}^{3} = \cos(\theta_1-\psi_1)\csc(\psi_1-\alpha_1); \\ \Omega_{4}^{2} & = \csc(\psi_1-\alpha_1);\ \Omega_{F_{l_2}}^{2} = \sin(\beta_1)\csc(\alpha_1-\psi_1);\ \Omega_{F_{r_2}}^{2} = 1; \\ \Omega_{Fk_{l_1}}^{2} & = \cos(\theta_1)\csc(\psi_1-\alpha_1); \\ \Omega_{6}^{1} & = \csc(\phi_1-\alpha_1);\ \Omega_{5}^{1} = \sin(\beta_1)\csc(\phi_1-\alpha_1);\ \Omega_{F_{l_2}}^{1} = 1; \\ \Omega_{F_{r_2}}^{1} & = \sin(\beta_1)\csc(\alpha_1-\phi_1);\ \Omega_{Fk_{r_1}}^{1} = \cos(\theta_1)\csc(\phi_1-\alpha_1) \end{cases} \tag{13}$$

From the above expressions of force coefficients, it is clear that the ones containing $\csc(\psi_i - \alpha_i)$ and $\csc(\phi_i - \alpha_i)$ can tend to infinity while their respective arguments approach zero. Physically, this happens when the joint i is near its flat singularities ($\alpha_i = \pm\pi$). Hence, to avoid unreasonably large forces in the bars, the designer must ensure that the joints operate within safe limits sufficiently far from these singular configurations, as detailed in Section 3.1.

The next step involves the computation of the bounds for the bar forces. From Eq. (12), it is observed that each term contains a product of a force and a force coefficient which depends on the configuration. A conservative estimation of the range of each of the terms can be obtained by firstly computing the bounds of the forces $[\underline{F}, \overline{F}]$ and the respective coefficients $[\underline{\Omega}, \overline{\Omega}]$. Then, the bounds of the product (ΩF) can be obtained as the minimum and maximum values of the set $\{\underline{\Omega}\ \underline{F}, \underline{\Omega}\overline{F}, \overline{\Omega}\underline{F}, \overline{\Omega}\ \overline{F}\}$. The range of forces and force coefficients are obtained as follows:

- Though the payload weight $F_{\mathrm{p}} = m_{\mathrm{p}}g$ (where $g = 9.8$ m/s^2 is the acceleration due to gravity), is a known constant, its bounds are assumed to be $F_{\mathrm{p}} \in [0, 2m_{\mathrm{p}}g]$. The lower bound is set to 0 to ensure that the manipulator remains safe even when it is loaded with a lighter payload than the assumed one. The upper bound is set to twice the actual weight to compensate for the masses of the bars and springs that were neglected. This is also expected to account for the dynamic forces that might arise while moving the manipulator. The bounds of other forces due to cables and the stiffness of the springs are also listed in the following ($i = 1, 2$):

$$\begin{cases} F_{\mathrm{p}} \in [0, 2m_{\mathrm{p}}g] \\ \{F_{l_i}, F_{r_i}\} \in [F_{\min}, F_{\max}] \\ \{k_i(l_{l_i} - l_{0_i}), k_i(l_{r_i} - l_{0_i})\} \in [0, k_i(l_{\max_i} - l_{0_i})] \end{cases} \tag{14}$$

- From Eq. (13), $\Omega_{\mathrm{p}}^{12}, \Omega_{\mathrm{p}}^{11}$ are functions of $(\alpha_1 + \alpha_2)$. Since $\alpha_i \in [-\alpha_{\max_i}, \alpha_{\max_i}]$, it follows that $(\alpha_1 + \alpha_2)$ must be bounded within $[-(\alpha_{\max_1} + \alpha_{\max_2}), (\alpha_{\max_1} + \alpha_{\max_2})]$. Hence, the bounding values of $\Omega_{\mathrm{p}}^{12}, \Omega_{\mathrm{p}}^{11}$ can be found by evaluating the respective cosine functions at the stationary points and the bounds. It is also apparent from Eq. (13) that one can reduce all the other force coefficients to functions of just one of the angles α_i. Thus, they can be classified into several categories as in Table 1, by studying them analytically (see Appendix A for illustrations). This classification aids in the computation of their bounding values. Note that while $\alpha_i = \alpha_{\max_i}$ (resp. $-\alpha_{\max_i}$), all the dependent angles $(\psi_i, \phi_i, \theta_i)$ in that joint attain their maximum (resp. minimum) values. Hence, the bounds of coefficients in categories II and III can be computed directly without rewriting them in terms of α_i.
- Once the bounds of distal bars F_{12}, F_{11} are found, they will be used successively for computing the bounds of F_{10}, F_9, F_8, and so on. This causes the force estimations to be increasingly more conservative as one moves toward the base. This computational feature is acceptable since the effect of neglected bar masses also increases as one moves closer to the base.
- Finally, the upper bounds of the estimated bar forces, denoted by F_j^*, will be used in Eq. (11) to compute the safe cross-section radius for bar j.

3.3.3. Practical considerations and symmetry of the manipulator

Let the value of r_{b_j} determined by substituting $F_{\text{critical}} = F_j^*$ in Eq. (11) be given by $r_{b_j}^*$. In order to avoid practical issues associated with the fabrication of small sections, a minimum cross-section radius $\underline{r_{b_j}} = 5$ mm is considered. Thus, a corrected

Table 1: Classification of the coefficients in Eq. (13) and computation of their bounds.

Category	Nature	Coefficients	Minimum	Maximum
I	Constant	$\Omega^7_{Fl_2}, \Omega^6_{Fl_2}, \Omega^5_7, \Omega^5_{Fr_2}, \Omega^4_7,$ $\Omega^4_{Fr_2}, \Omega^3_{Fr_2}, \Omega^2_{Fr_2}, \Omega^1_{Fl_2}$	Value of the constant	
II	Monotonic increase with $\alpha_i \in]-\pi, \pi[$	$\Omega^{10}_{11}, \Omega^{10}_{Fk_{l_2}}, \Omega^8_{Fk_{r_2}}, \Omega^7_{F_{r_2}},$ $\Omega^7_{k_{r_2}}, \Omega^5_8, \Omega^3_4, \Omega^3_{Fk_{l_1}}, \Omega^1_{Fk_{r_1}}$	Maximum angles	Minimum angles
III	Monotonic decrease with $\alpha_i \in]-\pi, \pi[$	$\Omega^9_{Fk_{l_2}}, \Omega^7_9, \Omega^5_{F_{l_2}}, \Omega^5_{k_{l_2}},$ $\Omega^3_{F_{l_2}}, \Omega^2_{Fk_{l_1}}$	Minimum angles	Maximum angles
IV	Possible extrema	$\Omega^{12}_{\text{p}}, \Omega^{11}_{\text{p}}, \Omega^9_{11}, \Omega^8_{12}, \Omega^6_9,$ $\Omega^6_{Fk_{r_2}}, \Omega^4_8, \Omega^4_{F_{l_2}}, \Omega^4_{k_{l_2}}, \Omega^2_4,$ $\Omega^2_{F_{l_2}}, \Omega^1_6, \Omega^1_5, \Omega^1_{F_{r_2}}$	Evaluate at stationary points, bounds; choose the minimum and maximum from them.	

cross-section radius is obtained as: $r_{b_j} = \max\left(\underline{r_{b_j}}, r^*_{b_j}\right)$.

Further, to preserve the mass symmetry of the manipulator about the configuration $(\alpha_1, \alpha_2) = (0, 0)$, it is necessary to have the same cross-sections for the following pairs of the bars (see Fig. 2(a)): $(1, 2)$, $(4, 6)$, $(8, 9)$, $(11, 12)$. This requirement is satisfied by setting the largest of the two cross-sections for both bars in each pair. Finally, the mass of j^{th} bar (m_j) can be computed as $m_j = \pi \rho r^2_{b_j} l_{b_j}$, where $\rho = 2700$ kg/m^3 is the volumetric density of Aluminum.

3.4. Static model of 2-X manipulator

As a first step, the total potential energy of the 2-X manipulator is computed to be:

$$U_{\text{x}} = m_{\text{p}} g y_p + \sum_{j=1}^{12} m_j g y_j + \sum_{i=1}^{2} \left(m_{k_i} g (y_{l_i} + y_{r_i}) + \frac{k_i}{2} \left((l_{l_i} - l_{0_i})^2 + (l_{r_i} - l_{0_i})^2 \right) + F_{l_i} l_{l_i} + F_{r_i} l_{r_i} \right) \tag{15}$$

where m_{p} is the mass of the point payload and y_p its y-coordinate, m_j represents the mass of the j^{th} bar (see Fig. 2(a) and Section 3.3) and y_j the y-coordinate of its geometric center. Similarly, m_{k_i} represents the mass of the springs in the i^{th} joint (see Eq. (4)), and y_{l_i} (resp. y_{r_i}) the y-coordinate of the mid-point of the attachment points of the left (resp. right) spring. In effect, the terms containing g represent the contribution of gravity in the total potential energy (assuming the zero-potential reference along the x-axis). The remaining terms signify the contribution of spring stiffness and actuation forces to the total potential, respectively. The lengths l_{l_i}, l_{r_i}, shown in Fig. 1(a), can be expressed as functions of l, b, α_i (see Eq. (1)). The forces F_{l_i}, F_{r_i} are the actuation forces imposed by cables C_{l_i}, C_{r_i} (see Fig. 2(b)), respectively, for $i = 1, 2$.

The static equilibrium equations can be obtained by setting the derivatives of U_{x} w.r.t. α_1 and α_2, to zeros. This results in two equations, which can be written in the following form:

$$\begin{cases} G_1(k_1, g, \alpha_1, \alpha_2) = \Gamma_1(F_{l_1}, F_{r_1}, \alpha_1) \\ G_2(k_2, g, \alpha_1, \alpha_2) = \Gamma_2(F_{l_2}, F_{r_2}, \alpha_2) \end{cases} \tag{16}$$

where G_i represents the wrench due to springs and gravity, while Γ_i is the wrench due to the actuating cables on the i^{th} joint, with $i = 1, 2$. The expressions of G_i and Γ_i are given by:

$$\begin{cases} G_1 = & -2C_{3\text{x}} \sin(\alpha_1 + \theta_2) \sqrt{l^2 - b^2 \cos^2(\theta_2)} + C_{1\text{x}} \sin\alpha_1 - C'_{3\text{x}} \sin(\alpha_1 + \alpha_2) \\ & + \frac{\sin(\theta_1)\left(-C''_{1\text{x}}\left(l^2 - 2b^2\cos^2(\theta_1)\right) - C'_{1\text{x}}\cos(\theta_1)\right)}{\sqrt{l^2 - b^2\cos^2(\theta_1)}} \\ G_2 = & C_{2\text{x}} \sin\alpha_2 - C'_{3\text{x}} \sin(\alpha_1 + \alpha_2) \\ & + \frac{C_{3\text{x}}\left(b^2 \sin(\theta_2)\cos(\theta_2)\cos(\alpha_1+\theta_2) + \sin(\alpha_1+\theta_2)\left(b^2\cos^2(\theta_2) - l^2\right)\right) - C'_{2\text{x}}\sin(\theta_2)\cos(\theta_2)}{\sqrt{l^2 - b^2\cos^2(\theta_2)}} \\ \Gamma_1 = & -bF_{l_1}\cos(\theta_1)\left(\frac{b\sin(\theta_1)}{\sqrt{l^2 - b^2\cos^2(\theta_1)}} - 1\right) - bF_{r_1}\cos(\theta_1)\left(\frac{b\sin(\theta_1)}{\sqrt{l^2 - b^2\cos^2(\theta_1)}} + 1\right) \\ \Gamma_2 = & -bF_{l_2}\cos(\theta_2)\left(\frac{b\sin(\theta_2)}{\sqrt{l^2 - b^2\cos^2(\theta_2)}} - 1\right) - bF_{r_2}\cos(\theta_2)\left(\frac{b\sin(\theta_2)}{\sqrt{l^2 - b^2\cos^2(\theta_2)}} + 1\right) \end{cases} \tag{17}$$

where $\theta_1 = (\alpha_1/2), \theta_2 = (\alpha_2/2)$ and

$$\begin{cases} C_{1\mathrm{x}} = 2b^2k_1 - ag(2m_{10} + 4m_{11} + 2m_4 + m_5 + 2m_7 + 4m_8 + 4m_{k_2} + 2m_\mathrm{p}) \\ C^{'}_{1\mathrm{x}} = 2b^2k_1l_{0_1} \\ C^{''}_{1\mathrm{x}} = g(m_1 + m_{10} + 2m_{11} + m_3 + 2m_4 + m_5 + m_7 + 2m_8 + m_{k_1} + 2m_{k_2} + m_\mathrm{p}) \\ C_{2\mathrm{x}} = 2b^2k_2 \\ C^{'}_{2\mathrm{x}} = 2b^2k_2l_{0_2} \\ C_{3\mathrm{x}} = g(m_{10} + 2m_{11} + m_8 + m_{k_2} + m_\mathrm{p}) \\ C^{'}_{3\mathrm{x}} = 2ag(m_{11} + m_\mathrm{p}) \end{cases} \tag{18}$$

The substitutions $\theta_1 = (\alpha_1/2), \theta_2 = (\alpha_2/2)$ have been made above and in the remaining sections for brevity. The masses (m_2, m_6, m_9, m_{12}) have been replaced by (m_1, m_4, m_8, m_{11}), respectively, owing to symmetry (see Fig. 2(a) and Section 3.3).

It can be shown that the coefficient of F_{l_i} (resp. F_{r_i}) in Eq. (17) is positive (resp. negative) when $\alpha_i \in]-\pi, \pi[$, with $i = 1, 2$ (see [18]). This implies that F_{l_i} imposes a counterclockwise moment and F_{r_i} imposes a clockwise moment on the i^{th} joint, respectively. This feature is also evident from the cable routing shown in Fig. 2(b). Thus, an increase in the force F_{r_i} means that F_{l_i} also increases to preserve the configuration of the manipulator. This simultaneous increase (or decrease) of the antagonistic forces allows the manipulator to achieve different stiffnesses at the same configuration, making them suitable for applications requiring variable stiffness.

Recall that the actuation forces imposed by cables are limited by: $F_{l_i}, F_{r_i} \in [F_\mathrm{min}, F_\mathrm{max}]$. Thus, at a given configuration (α_1, α_2), the actuation wrench Γ_i is bounded below by $\underline{\Gamma_i}$ which occurs when ($F_{l_i} = F_\mathrm{min}$ and $F_{r_i} = F_\mathrm{max}$), and bounded above by $\overline{\Gamma_i}$ which occurs when ($F_{l_i} = F_\mathrm{max}$ and $F_{r_i} = F_\mathrm{min}$), for $i = 1, 2$. Consequently, the equilibrium equation given in Eq. (16) can be satisfied at (α_1, α_2) only when $G_i \in \left[\underline{\Gamma_i}, \overline{\Gamma_i}\right]$, which are known as the wrench-feasibility conditions.

The stability of an equilibrium configuration can be characterized by the positive definiteness of the associated stiffness matrix. For the 2-X manipulator, the articular stiffness matrix ($\mathbf{K}_\alpha$) can be computed as the Hessian of its potential energy w.r.t. $[\alpha_1, \alpha_2]^\top$ (see [24]), as follows:

$$\mathbf{K}_\alpha = \begin{pmatrix} K_{11} & K_{12} \\ K_{12} & K_{22} \end{pmatrix} \text{ with } K_{11} = \frac{4K^{'}_{11}}{\left(\lambda^2 - c_1^2\right)^{3/2}} \text{ and } K_{22} = \frac{4K^{'}_{22}}{\left(\lambda^2 - c_2^2\right)^{3/2}} \tag{19}$$

where

$$\begin{cases} K^{'}_{11} = & -4b^4c_{12}C_{3\mathrm{x}}\left(\lambda^2 - c_1^2\right)^{3/2}\sqrt{\lambda^2 - c_2^2} - b^4c_1C^{''}_{1\mathrm{x}}\left\{2c_1^4 - c_1^2\left(3\lambda^2 + 2s_1^2\right) + \lambda^4 + 3\lambda^2s_1^2\right\} \\ & +b^2C^{'}_{1\mathrm{x}}\left(c_1^4 - c_1^2\lambda^2 + \lambda^2s_1^2\right) - 2b^3c'_{12}C^{'}_{3\mathrm{x}}\left(\lambda^2 - c_1^2\right)^{3/2} + 2b^3C_{1\mathrm{x}}\left(\lambda^2 - c_1^2\right)^{3/2}\left(c_1^2 - s_1^2\right) \\ & -b^4F_{r_1}\left\{s_1\left(\lambda^2 - c_1^2\right)^{3/2} + \left(c_1^4 - c_1^2\lambda^2 + \lambda^2s_1^2\right)\right\} + b^4F_{l_1}\left\{s_1\left(\lambda^2 - c_1^2\right)^{3/2} - \left(c_1^4 - c_1^2\lambda^2 + \lambda^2s_1^2\right)\right\} \\ K^{'}_{22} = & -b^4C_{3\mathrm{x}}\left\{c_{12}\left(2c_2^4 - 3c_2^2\lambda^2 + \lambda^4 + \lambda^2s_2^2\right) + 2c_2s_{12}s_2\left(\lambda^2 - c_2^2\right)\right\} \\ & -2b^3c'_{12}C^{'}_{3\mathrm{x}}\left(\lambda^2 - c_2^2\right)^{3/2} + 2b^3C_{2\mathrm{x}}\left(\lambda^2 - c_2^2\right)^{3/2}\left(c_2^2 - s_2^2\right) + b^2C^{'}_{2\mathrm{x}}\left(c_2^4 - c_2^2\lambda^2 + \lambda^2s_2^2\right) \\ & -b^4F_{r_2}\left\{s_2\left(\lambda^2 - c_2^2\right)^{3/2} + \left(c_2^4 - c_2^2\lambda^2 + \lambda^2s_2^2\right)\right\} + b^4F_{l_2}\left\{s_2\left(\lambda^2 - c_2^2\right)^{3/2} - \left(c_2^4 - c_2^2\lambda^2 + \lambda^2s_2^2\right)\right\} \\ \\ K_{12} = & -8C^{'}_{3\mathrm{x}}c'_{12} + \frac{4b}{\sqrt{\lambda^2 - c_2^2}}\left[C_{3\mathrm{x}}\left\{c'_{12}c_2 - s'_{12}s_2 - \left(2\lambda^2 - 1\right)c_{12}\right\}\right] \end{cases} \tag{20}$$

in which $\lambda = (l/b), c_1 = \cos(\theta_1), s_1 = \sin(\theta_1), c_2 = \cos(\theta_2), s_2 = \sin(\theta_2), s_{12} = \sin(2\theta_1 + \theta_2), c_{12} = \cos(2\theta_1 + \theta_2), c'_{12} = \cos(2(\theta_1 + \theta_2)), s'_{12} = \sin(2(\theta_1 + \theta_2))$.

Since the equilibrium equations in Eq. (16) must be satisfied while evaluating the stiffness, one could solve for two of the forces, say, (F_{l_1}, F_{l_2}) from the two equations and substitute in Eq. (20). This results in the stiffness matrix $\mathbf{K}^{\mathrm{rr}}_\alpha$ which contains only the redundant actuation forces (F_{r_1}, F_{r_2}):

$$\mathbf{K}^{\mathrm{rr}}_\alpha = \begin{pmatrix} K^{\mathrm{rr}}_{11} & K_{12} \\ K_{12} & K^{\mathrm{rr}}_{22} \end{pmatrix} \text{ with } K^{\mathrm{rr}}_{11} = \frac{4K^{\mathrm{rr}'}_{11}}{bc_1\left(\lambda^2 - c_1^2\right)} \text{ and } K^{\mathrm{rr}}_{22} = \frac{4K^{\mathrm{rr}'}_{22}}{bc_2\left(\lambda^2 - c_2^2\right)} \tag{21}$$

where

$$\begin{cases} K_{11}^{\mathrm{rr}'} = & -2b^2C_{3\mathrm{x}}\sqrt{\lambda^2-c_2^2}\left(2c_1c_{12}\left(\lambda^2-c_1^2\right)+c_1^2s_{12}\sqrt{\lambda^2-c_1^2}+\lambda^2s_1s_{12}\right) \\ & +b^2C_{1\mathrm{x}}^{''}\left\{2c_1^4s_1-c_1^2\lambda^2s_1+\sqrt{\lambda^2-c_1^2}\left(2c_1^4-2c_1^2s_1^2-\lambda^2\right)\right\} \\ & +bC_{3\mathrm{x}}^{'}\left\{2c_1c_{12}'\left(c_1^2-\lambda^2\right)-c_1^2s_{12}'\sqrt{\lambda^2-c_1^2}-\lambda^2s_1s_{12}'\right\} \\ & +2bc_1^3C_{1\mathrm{x}}\left(s_1\sqrt{\lambda^2-c_1^2}-c_1^2+\lambda^2+s_1^2\right)-c_1^3C_{1\mathrm{x}}^{'}\left(\sqrt{\lambda^2-c_1^2}+s_1\right) \\ & +2b^2c_1^3F_{r_1}\left(\sqrt{\lambda^2-c_1^2}+s_1\right) \\ K_{22}^{\mathrm{rr}'} = & b^2C_{3\mathrm{x}}\left[c_{12}c_2\left\{c_2^2\left(2\sqrt{\lambda^2-c_2^2}+s_2\right)-\lambda^2\sqrt{\lambda^2-c_2^2}\right\}+s_{12}\left\{c_2^4-c_2^2\left(2s_2\sqrt{\lambda^2-c_2^2}+\lambda^2\right)-\lambda^2s_2\sqrt{\lambda^2-c_2^2}\right\}\right] \\ & +C_{3\mathrm{x}}^{'}\left\{2bc_{12}'c_2\left(c_2^2-\lambda^2\right)-bs_{12}'\left(c_2^2\sqrt{\lambda^2-c_2^2}+\lambda^2s_2\right)\right\} \\ & +2bc_2^3C_{2\mathrm{x}}\left(s_2\sqrt{\lambda^2-c_2^2}-c_2^2+\lambda^2+s_2^2\right)-c_2^3C_{2\mathrm{x}}^{'}\left(\sqrt{\lambda^2-c_2^2}+s_2\right) \\ & +2b^2c_2^3F_{r_2}\left(\sqrt{\lambda^2-c_2^2}+s_2\right) \end{cases} \tag{22}$$

From the above expressions, one finds that the redundant force F_{r_i} is present only in the i^{th} diagonal term. Additionally, its coefficient $\frac{4\left(2b^2c_i^3\left(\sqrt{\lambda^2-c_i^2}+s_i\right)\right)}{bc_i(\lambda^2-c_i^2)}$ is always positive while $\lambda > 1$ (assembly condition which is always valid) and $\theta_i \in \left]-\frac{\pi}{2}, \frac{\pi}{2}\right[$ within the flat singularities, for $i = 1, 2$. This shows that the antagonist forces have a positive correlation with the stiffness for the 2-X manipulator, similar to that of a single X-joint [18]. Hence, maximum stiffness at a given configuration can be obtained by setting maximum forces in the cables such that all of them are within their bounds $[F_{\min}, F_{\max}]$. Since there are two redundant actuators in this manipulator, a pair of forces (F_{r_1}, F_{r_2}) or (F_{r_1}, F_{l_2}) or (F_{l_1}, F_{r_2}) or (F_{l_1}, F_{l_2}) can be set to $F_{\max}$ to obtain maximum stiffness at any configuration.

Suppose a given configuration permits setting the forces (F_{r_1}, F_{r_2}) to $F_{\max}$, the stiffness matrix corresponding to maximum stiffness can be obtained as $\overline{\mathbf{K}}_{\alpha}^{\mathrm{rr}} = \mathbf{K}_{\alpha}^{\mathrm{rr}}(F_{r_1} = F_{\max}, F_{r_2} = F_{\max})$ from Eqs. (21),(22). If the resulting matrix is positive-definite, then that configuration is a stable one, otherwise it is not. However, while the configuration is not known a priori, the maximum stiffness could occur when any one of the four pairs of forces is at $F_{\max}$. Thus, the expressions for stiffness matrices corresponding to each force pair at $F_{\max}$ are computed beforehand. They are denoted by $\left(\overline{\mathbf{K}}_{\alpha}^{\mathrm{rr}}, \overline{\mathbf{K}}_{\alpha}^{\mathrm{rl}}, \overline{\mathbf{K}}_{\alpha}^{\mathrm{lr}}, \overline{\mathbf{K}}_{\alpha}^{\mathrm{ll}}\right)$. The limiting condition(s) of stability can be found from the vanishing of the determinants of these matrices as explained in [32],[33]. Their zero-level sets can be plotted in the joint space to distinguish between the stable and unstable configurations for the manipulator. Note that if a configuration (α_1, α_2) is identified as stable, then at least one combination actuation forces can stabilize the manipulator at that configuration.

The set of all (α_1, α_2) inside the actual joint limits, which respect the conditions of wrench-feasibility and stability, forms the stable wrench-feasible joint space (SWFJ) for this manipulator. The corresponding set of all end-effector positions in the task space (x, y) forms the SWFW. In order to map the SWFJ onto the task space, the kinematic model of the 2-X manipulator is essential and is derived in the next section.

3.5. *Kinematic model of 2-X manipulator*

The kinematic model of the 2-X manipulator involves expressing the end-effector coordinates (x, y) in terms of the joint angles (α_1, α_2). Considering that $\alpha_i \in]-\pi, \pi[, i = 1, 2$, it is possible to present the direct kinematics of the manipulator (see Fig. 1(a)) as follows (see [34] for more details):

$$\begin{cases} x = -l_1(\alpha_1)\sin(\alpha_1/2) - a(\sin\alpha_1 + \sin(\alpha_1+\alpha_2)) - l_2(\alpha_2)\sin(\alpha_1+\alpha_2/2) \\ y = l_1(\alpha_1)\cos(\alpha_1/2) + a(\cos\alpha_1 + \cos(\alpha_1+\alpha_2)) + l_2(\alpha_2)\cos(\alpha_1+\alpha_2/2) \\ \text{where } l_i(\alpha_i) = \sqrt{l^2 - b^2\cos^2(\alpha_i/2)}, \quad i = 1, 2 \end{cases} \tag{23}$$

Differentiation w.r.t. time yields:

$$\begin{bmatrix} \dot{x} \\ \dot{y} \end{bmatrix} = \mathbf{J}_{\mathrm{x}} \begin{bmatrix} \dot{\alpha}_1 \\ \dot{\alpha}_2 \end{bmatrix}, \text{where } \mathbf{J}_{\mathrm{x}} = \begin{bmatrix} \frac{\partial x}{\partial \alpha_1} & \frac{\partial x}{\partial \alpha_2} \\ \frac{\partial y}{\partial \alpha_1} & \frac{\partial y}{\partial \alpha_2} \end{bmatrix} \text{ is a Jacobian matrix.} \tag{24}$$

The singularity condition for the manipulator is obtained from the vanishing of the determinant of $\mathbf{J}_{\mathrm{x}}$. After clearing the non-zero factors and the denominator of $\det(\mathbf{J}_{\mathrm{x}})$, the singularity condition can be expressed as [34]:

$$\begin{aligned} & 4a\sin\theta_2\sqrt{l^2-b^2\cos^2\theta_1}\left(l^2-2b^2\cos^2\theta_2\right)+2b^4\cos\theta_1\sin\theta_2\cos^2\theta_2 \\ & +b^2l^2\left(\sin(\theta_1-\theta_2)-2\cos^2\theta_2\sin(\theta_1+\theta_2)\right)+l^4\sin(\theta_1+\theta_2) \\ & +\sqrt{l^2-b^2\cos^2\theta_2}\left(2a\left(\cos\theta_1\sin\alpha_2\left(l^2-b^2\right)-l^2\sin\theta_1\sin^2\theta_2+l^2\sin\theta_1\cos^2\theta_2\right)\right. \\ & \left.-\left(b^2-4a^2\right)\sin\alpha_2\sqrt{l^2-b^2\cos^2\theta_1}\right)=0 \end{aligned} \tag{25}$$

where $\theta_1 = (\alpha_1/2), \theta_2 = (\alpha_2/2)$. Note that $(\alpha_1, \alpha_2) = (0, 0)$ satisfies the singularity condition irrespective of the bar lengths.

The SWFW boundary is obtained by mapping the boundary of the SWFJ onto the task space using Eq. (24). Additionally, it is also necessary to map the singular configurations inside SWFJ separately, as they form an essential part of the SWFW boundary.

The steps involved in the computation of SWFJ and SWFW are discussed briefly in the next section.

3.6. Stable wrench-feasible workspace of 2-X manipulator

When all the parameters (bar dimensions, springs, cable forces) of the 2-X manipulator are defined, its SWFW can be obtained by using the method described in [32],[33]. The important steps involved are summarized in the following:

1. All the limiting conditions of wrench-feasibility and stability, namely, $\Big\{G_1 - \underline{\Gamma_1} = 0,\ G_1 - \overline{\Gamma_1} = 0,\ G_2 - \underline{\Gamma_2} = 0,\ G_2 - \overline{\Gamma_2} = 0,\ \det\left(\overline{\mathbf{K}}_\alpha^{\mathrm{rr}}\right) = 0,\ \det\left(\overline{\mathbf{K}}_\alpha^{\mathrm{rl}}\right) = 0,\ \det\left(\overline{\mathbf{K}}_\alpha^{\mathrm{lr}}\right) = 0,\ \det\left(\overline{\mathbf{K}}_\alpha^{\mathrm{ll}}\right) = 0\Big\}$, must be consolidated together into a vector $\boldsymbol{f}(\alpha_1, \alpha_2) = \mathbf{0}$.
2. These conditions must be rewritten as polynomials in $t_1 = \tan(\alpha_1/4)$ (resp. $t_2 = \tan(\alpha_2/4)$) by suppressing the variable α_2 (resp. α_1) inside its coefficients to obtain $\boldsymbol{f}_1(t_1) = \mathbf{0}$ (resp. $\boldsymbol{f}_2(t_2) = \mathbf{0}$).
3. The joint space (α_1, α_2) must be discretized into grid lines of α_1 and α_2 inside the joint limits.
4. On each grid line of α_1 (resp. α_2), the bounding values of the stable wrench-feasible intervals of α_2 (resp. α_1) can be determined by solving the univariate polynomial $\boldsymbol{f}_2(t_2) = \mathbf{0}$ (resp. $\boldsymbol{f}_1(t_1) = \mathbf{0}$). The spurious solutions (if any) must be eliminated.
5. Once the boundary points (α_1, α_2) of the SWFJ on all the grid lines are calculated, a linear interpolation must be performed between them to obtain polygon(s) approximating the actual SWFJ.
6. Finally, all the boundary points of SWFJ, along with the manipulator singularities, must be mapped onto the task space using the direct kinematic model (see Eq. (23)) to obtain the corresponding polygonal approximation of the SWFW.

3.7. Consolidation of all design conditions and a numerical example for 2-X manipulator

In this section, all the design considerations discussed above for the 2-X manipulator are consolidated to determine its SWFW and a numerical example is presented. Starting from a given design of the 2-X manipulator, i.e., with defined geometry (b, l, a), safe joint limits $(\overline{\alpha_{\max}})$, springs (k_i, σ_i) for $i = 1, 2$, and maximal actuation force $(F_{\max})$, the steps involved in the computation of its SWFW are presented in a flow chart in Fig. 8. As a numerical illustration, consider the following design of the 2-X manipulator: $b = 0.2$ m, $l = 0.4$ m, $a = 0.5$ m, $\overline{\alpha_{\max}} = 5\pi/6$ rad, $k_1 = 3000$ N/m, $\sigma_{k_1} = 1.0$, $k_2 = 1000$ N/m, $\sigma_{k_2} = 0.7$, $F_{\max} = 200$ N. A payload of $m_{\mathrm{p}} = 2$ kg is considered at the end-effector. The SWFJ and SWFW obtained for this design are presented in Figs. 9(a) and 9(b), respectively. The steps involved are described in the following:

- **Section 3.2**: The first step involves the computation of the feasible design space for each of the springs and determining the dependent parameters. If the feasible design space is empty for any of the springs, then the design of that 2-X manipulator is deemed infeasible. The spring stiffnesses were chosen such that the manipulator is in stable equilibrium at $(\alpha_1, \alpha_2) = (0, 0)$ without actuation forces. For spring 1, $k_1 = 3000$ N/m, $\sigma_{k_1} = 1.0$, the dependent parameters are found to be (see Fig. 6(b) and Eqs. (5),(6),(2),(4)): $d = 6.0$ mm, $D = 58.4844$ mm, $N_a = 22.0005, l_{0_1} = 0.2430$ m, $l_{\max_1} = 0.4939$ m, $m_{k_1} = 1.0195$ kg. Similarly, for spring 2, $k_2 = 1000$ N/m, $\sigma_{k_2} = 0.7$, the parameters are found to be: $d = 4.7$ mm, $D = 52.3495$ mm, $N_a = 34.6515, l_{0_2} = 0.2629$ m, $l_{\max_2} = 0.4565$ m, $m_{k_2} = 0.8433$ kg. The total mass contributed by all the springs are found to be $4(m_{k_1} + m_{k_2}) = 3.7257$ kg.

- **Section 3.1**: By substituting the spring free length data in Eq. (2), one obtains $\alpha_{\max_1} = 1.3561$ rad and $\alpha_{\max_2} = 1.0108$ rad, i.e., the actual range of movement of the two joints are $\alpha_1 = [-1.3561, 1.3561]$ rad and $\alpha_2 \in [-1.0108, 1.0108]$ rad, respectively.

- **Section 3.3**: The conservative bounds for bar forces are computed using the data of geometry, maximal actuation force $F_{\max}$, springs, and payload. The numerical values are presented in the second column of Table 2. The safe cross-section radii for the bars and their corrected values based on symmetry and assumed minimum $\underline{r_{b_j}} = 5$ mm are presented in the subsequent columns. Further, the respective masses (m_j) for all the bars have also been presented. The total mass contributed by the moving bars is 1.4956 kg, which is much smaller than those of the springs (3.7257 kg). The total moving mass of the manipulator is found to be 5.224 kg.

- **Section 3.4**: The static model of the manipulator (Eqs. (17),(18),(19),(20)) can be defined using the data of springs, bar masses, and geometry of the manipulator obtained previously.

- **Section 3.5**: Independent of the above computations, the direct kinematic model and the singularity condition $\det(\mathbf{J}_{\mathrm{x}}) = 0$ can be defined using the geometry parameters (b, l, a).

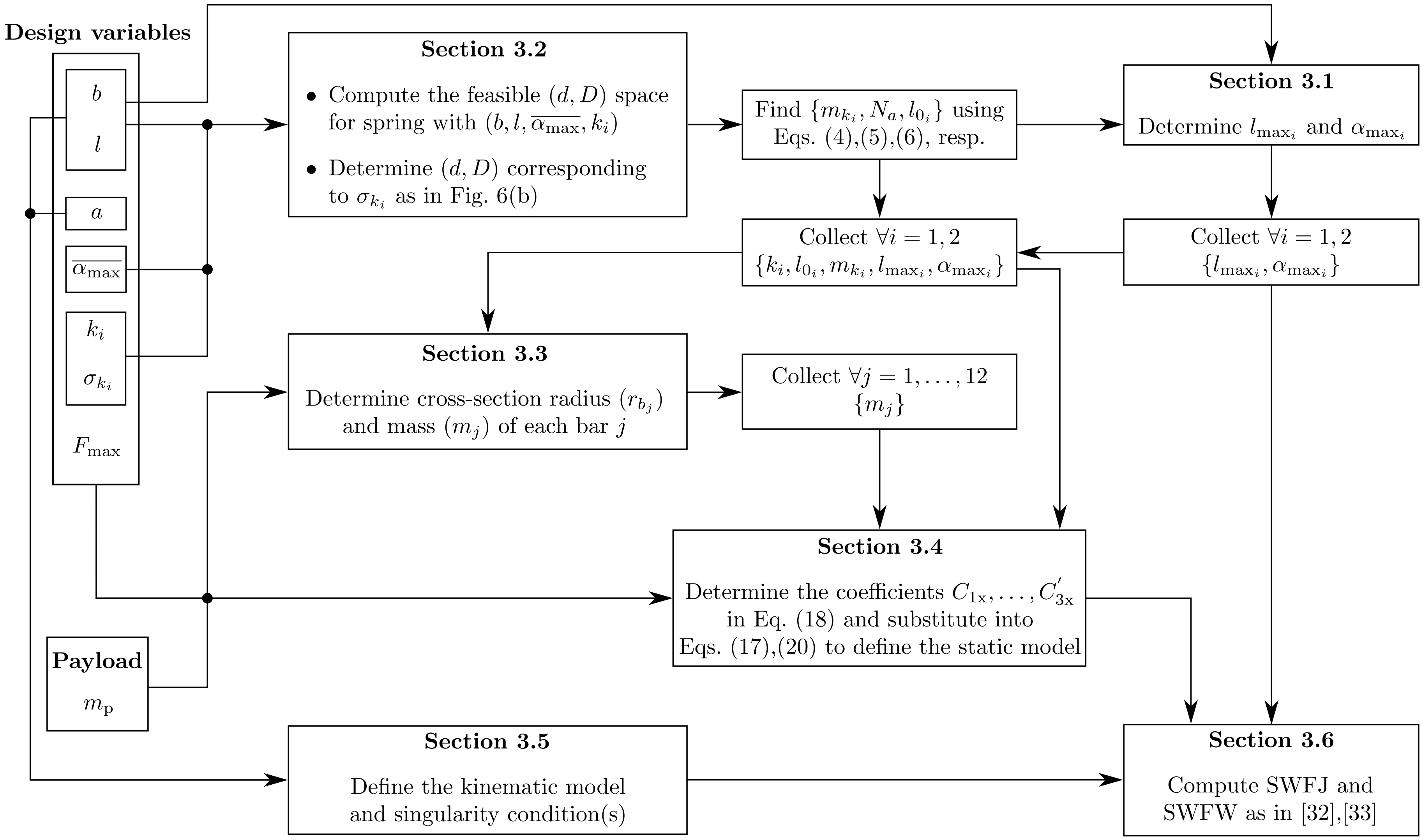

Figure 8: Computational scheme for the determination of SWFW for the 2-X manipulator that accounts for all of its design considerations discussed in Section 3.

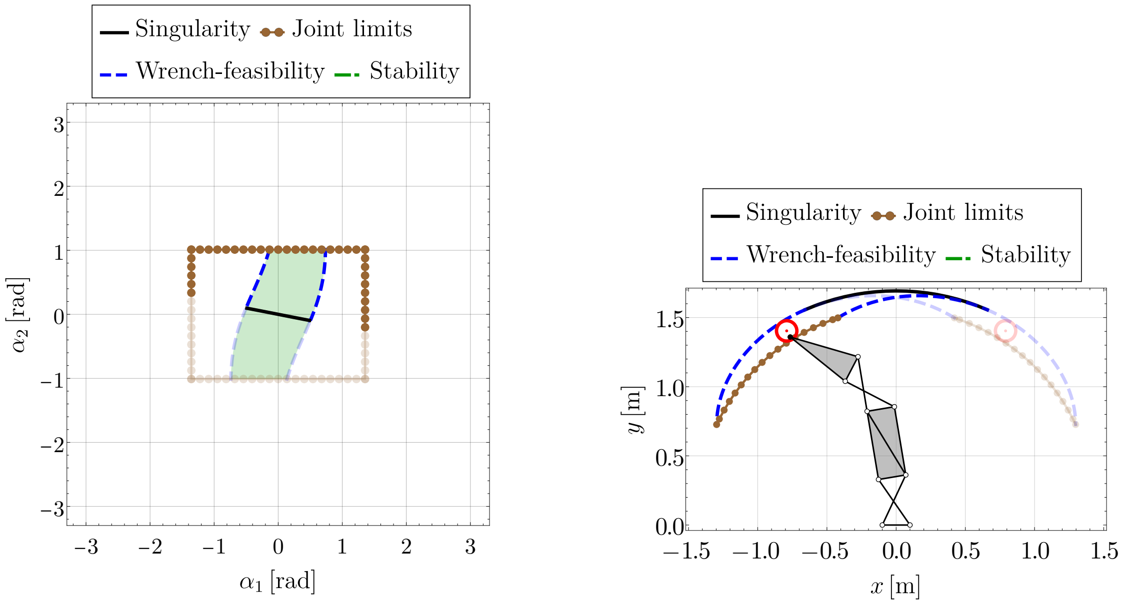

(a) SWFJ highlighted in shading

(b) SWFW with two maximal inscribed disks (of radius 0.0736 m each)

Figure 9: Stable wrench-feasible joint space (SWFJ) and stable wrench-feasible workspace (SWFW) for the 2-X manipulator with: $b = 0.2$ m, $l = 0.4$ m, $a = 0.5$ m, $\overline{\alpha_{\max}} = 5\pi/6$ rad, $k_1 = 3000$ N/m, $l_{0_1} = 0.2430$ m, $m_{k_1} = 1.0195$ kg, $k_2 = 1000$ N/m, $l_{0_2} = 0.2629$ m, $m_{k_2} = 0.8433$ kg, $F_{\max} = 200$ N. In SWFJ, the curves lying in the region where $\det(\mathbf{J}_x) > 0$ are shown in opaque style while those in $\det(\mathbf{J}_x) < 0$ region are shown in transparent style. The images of these curves in the task space are also shown in the same style for the sake of clarity.

Table 2: 2-X manipulator: Range of estimated buckling loads and the resulting safe cross-section radii for the bars along with their masses.

Bar index	**Estimated load** [N]	**Cross-section radius** [mm]		**Mass** [kg]
j		Computed ($r^*_{b_j}$)	Corrected (r_{b_j})	m_j
12	[-101.92, 101.92]	2.64	5.00	0.1081
11	[-101.92, 101.92]	2.64		
10	[-461.71, 162.19]	1.86	5.00	0.0424
9	[-173.81, 772.84]	3.89	5.00	0.0848
8	[-173.81, 772.84]	3.89		
7	[-726.05, 807.06]	2.78	5.00	0.0424
5	[-4128.03, 4128.03]	6.85	6.85	0.2146
6	[-567.46, 958.53]	4.58	6.60	0.1845
4	[-4091.47, 4107.72]	6.60		
3	[-8434.49, 8240.10]	4.96	5.00	0.0424
2	[-9041.49, 10451.80]	7.45	7.70	0.2010
1	[-9694.20, 11896.80]	7.70		

Total bar mass	1.4986
Mass of springs ($2(m_{k_1} + m_{k_2})$)	3.7257
Total moving mass of the manipulator	5.2244

- **Section 3.6**: Using the static model and joint limits ($\alpha_{\max_i}$) for all joints $i = 1, 2$, the SWFJ of the manipulator can be constructed as in Fig. 9(a) (shaded part). In this example, it is observed that the limiting boundaries of SWFJ are only formed by the wrench-feasibility and joint limits but not by stability. This indicates that the manipulator must possess good stiffness throughout the SWFJ. Further, the bounding points of SWFJ and singularities in the joint space have been mapped onto the task space using the direct kinematic map in Eq. (23). The resulting plot of the SWFW of the manipulator is shown in Fig. 9(b).

In Fig. 9(a), all the curves in the region $(\det(\mathbf{J}_x) > 0)$ (resp. region $(\det(\mathbf{J}_x) < 0)$) are shown in opaque (resp. transparent) styles, to distinguish between the two symmetric halves in the joint space and display the overlapping regions in task space with clarity. As expected from the manipulator symmetry, the images of the two halves of SWFJ in the task space, are symmetric about the y-axis. The overlapping region around the y-axis has two feasible configurations, while those on the two farther sides have just one feasible configuration. Due to the symmetry of SWFW, it is sufficient to use just one half (e.g., opaque style) to quantify its size. In the literature, it is a common strategy to inscribe a regular shape, such as a disk, inside the workspace and use its dimensions for quantification [35]. Since the SWFW is in the form of polygons [32], an open-source `c++` library `polylabel` has been used to find the maximally inscribed disk(s) inside it[4]. The inscribed disks shown in Fig. 9(b) have a radius of 0.0736 m each. For this design, it takes about 43 ms (averaged over 100 runs) to compute the SWFW and the maximally inscribed disk[5]. The maximal vertical reach (i.e., the y-coordinate of the end-effector while the joint angles are $(\alpha_1, \alpha_2) = (0, 0)$) of the manipulator is 1.6928 m, which is about 23 times the radius of the inscribed disk.

As a validation of the obtained design, it has been verified that the actual loads induced in the bars are less than the estimated ones at several configurations (α_1, α_2) inside the SWFJ and for several combinations of actuation forces $\in [F_{\min}, F_{\max}]$ in Appendix B. This study confirms that the design of the 2-X manipulator proposed is safe from buckling failure for manipulating a payload of 2 kg inside its SWFW. Note that the resulting mass of the bars and springs (5.2244 kg) is more than twice the payload mass assumed in the design process in Section 3.3.2. But, the actual forces induced in the bars are much smaller than the estimated ones. This difference can be attributed to the further overestimation in the scheme, where the worst combinations of all forces and the respective force coefficients were considered. It is observed that this difference also increases as one moves from the end-effector toward the base. This is due to the overestimation of forces at the distal bars and their recursive substitutions in the computation of forces in the proximal bars (see Eq. (12)). Nevertheless, the resulting cross-sections of the bars are not impacted severely due to this overestimation, as observed from Table 2, thanks to the damping exponent $(1/4)$ in Eq. (11). It was verified through several numerical examples that the resulting bar cross-sections are safe for the 2-X manipulator, thereby validating the proposed methodology.

The design considerations for the 2-R manipulator and the computation of its SWFW will be discussed in the following section.

4. Design considerations for 2-R manipulator

The schematic of the 2-R manipulator with bar and pivot labels is shown in Fig. 10(a). This manipulator is also *remotely* actuated with four motors using one cable each, as shown in Fig. 10(b). The cables C_{l_i} and C_{r_i} actuate the i^{th} joint *independently*, for $i = 1, 2$, as explained in the case of 2-X manipulator (see Section 3).

In the following, we describe the different factors to be considered in the design of 2-R manipulators. The joint limits of an R-joint are explored in Section 4.1. The governing conditions for spring design are listed in Section 4.2. The estimation of buckling loads for the bars and the determination of their cross-section radii are carried out in Section 4.3. The static and kinematic models of the 2-R manipulator are developed in Sections 4.4 and 4.5, respectively. Finally, the SWFW computation is illustrated with an example in Section 4.6.

4.1. Joint limits for i^{th} R-joint

The movement of an R-joint is limited due to cable actuation in two different ways. First, due to the vanishing of the segment joining the cables (i.e., meeting of the pivots (B_{l_i} and P_{l_i}) or (B_{r_i} and P_{r_i})). Second, due to force-closure singularity [36], which occurs when the line of action of force passes through the center of rotation (i.e., when (B_{l_i}, O_i, P_{l_i}) or (B_{r_i}, O_i, P_{r_i}) become collinear). For the R-joint, it can be shown that the joint limits will be formed by the first condition when $(r > h)$ and by the second condition when $(r < h)$, and by both of them simultaneously when $(r = h)$ (see [18]). In these cases, the upper bound for joint limits ($\overline{\overline{\alpha_{\max}}}$) are given by:

$$\overline{\overline{\alpha_{\max}}} = \begin{cases} 2\arctan\left(h/r\right), & \text{if } r > h \\ 2\arctan\left(r/h\right), & \text{if } r < h \\ \frac{\pi}{2}, & \text{if } r = h \end{cases} \tag{26}$$

---

[4] The associated code could be found at `https://github.com/mapbox/polylabel`.

[5] All the computations reported in this work have been performed on a computer with an Intel® Core™ i7-6700 CPU running @ 3.40GHz processor, using a `C++` code.

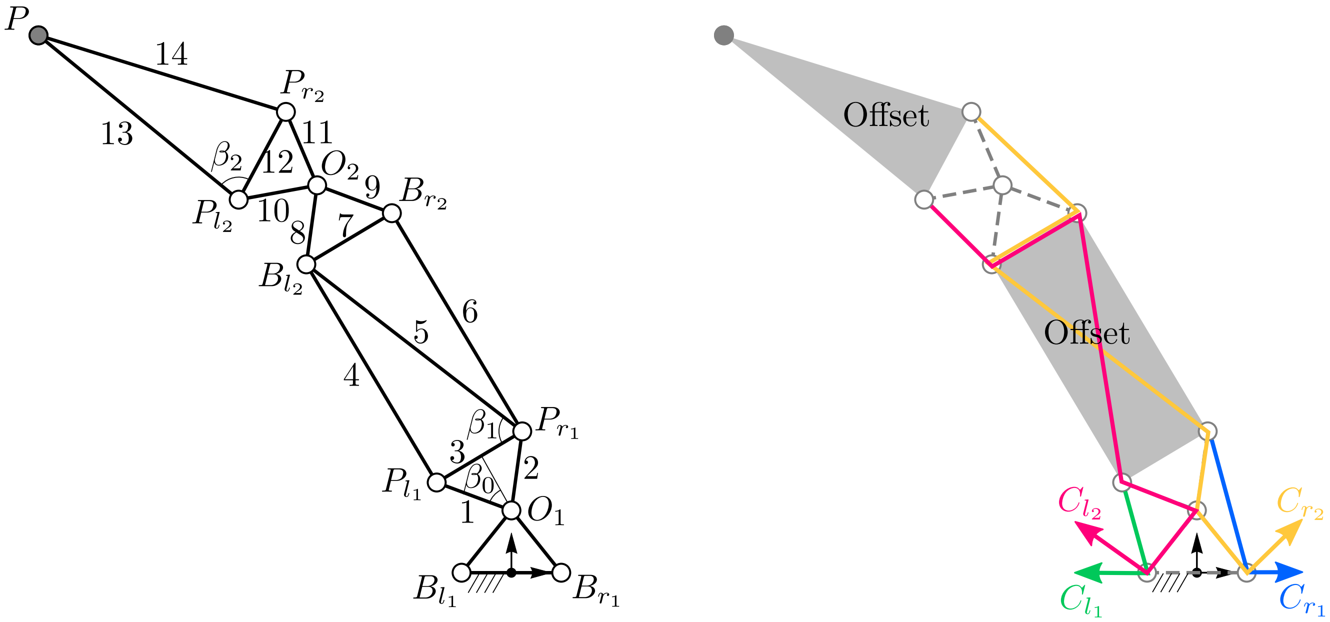

(a) Bar labels (b) Cable routing

Figure 10: Bar labels (left) and cable routing scheme (right) for the 2-R manipulator.

As in the case of X-joint, a safe amplitude of movement should be defined by the designer as $\overline{\alpha_{\max}}$ which is strictly less than $\overline{\overline{\alpha_{\max}}}$. However, unlike in the X-joint, the singularities occur at different joint angles depending on the geometry of the joint. Hence, it is more convenient to define the safe limits as a fraction of the bounds due to singularity, i.e., $\overline{\alpha_{\max}} = \sigma_\alpha \overline{\overline{\alpha_{\max}}}$, with $\sigma_\alpha \in]0,1[$, such that it is valid for all joint geometries.

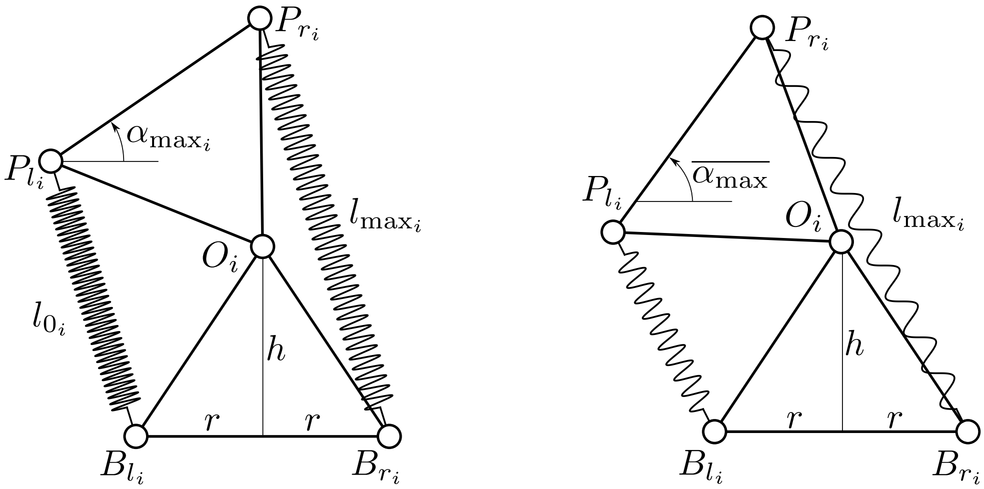

(a) Case A: $l_{l_i}(\overline{\alpha_{\max}}) < l_{0_i} < 2h$ (b) Case B: $0 < l_{0_i} \leq l_{l_i}(\overline{\alpha_{\max}})$

Figure 11: Joint limits of an R-joint depending on the spring free length (l_{0_i}) and bar lengths.

Further, for the i^{th} R-joint, the actual joint limits ($\pm\alpha_{\max_i}$) can differ from the safe joint limits ($\pm\overline{\alpha_{\max}}$) depending on the free length (l_{0_i}) of the springs installed in it (see Fig. 11). Since identical springs are used on the two sides of the joint, it is apparent that their free length must respect $l_{0_i} \in [0, 2h]$ for installation. The lengths of the springs on either side (i.e., the distance between their attachment points) are given by (see [18]):

$$l_{l_i}(\alpha_i) = 2\left(h\cos\left(\frac{\alpha_i}{2}\right) - r\sin\left(\frac{\alpha_i}{2}\right)\right) \qquad l_{r_i}(\alpha_i) = 2\left(h\cos\left(\frac{\alpha_i}{2}\right) + r\sin\left(\frac{\alpha_i}{2}\right)\right) \tag{27}$$

The computation of actual joint limit ($\alpha_{\max_i}$) and maximum operating length ($l_{\max_i}$) of the springs is carried out in a case-wise manner in the following:

- **Case A** $[(l_{l_i}(\overline{\alpha_{\max}}) < l_{0_i} < 2h)$ in Fig. 11(a)]: In this case, $\alpha_{\max_i}$ is attained when the left spring reaches its free length (l_{0_i}). At this configuration, the right spring attains its maximum operating length ($l_{\max_i}$). From the geometry of

R-joint, $\alpha_{\max_i}$ and $l_{\max_i}$ can be obtained in terms of l_{0_i} as:

$$\begin{cases} \alpha_{\max_i} = 2\left(\arccos\left(\frac{l_{0_i}}{2\sqrt{h^2+r^2}}\right) - \arccos\left(\frac{h}{\sqrt{h^2+r^2}}\right)\right) \\ l_{\max_i} = \frac{2hr\sqrt{4(h^2+r^2)-l_{0_i}^2}+l_{0_i}\left(h^2-r^2\right)}{h^2+r^2} \end{cases} \tag{28}$$

- **Case B** $[0 < l_{0_i} \leq l_{l_i}(\overline{\alpha_{\max}})$ in Fig. 11(b)]: In this case, the joint movement is limited by the safe limits, i.e., $\alpha_{\max_i} = \overline{\alpha_{\max_i}}$, irrespective of the spring free length. The maximum operating length of the springs is also attained at these limits, as computed by:

$$\begin{cases} \alpha_{\max_i} = \overline{\alpha_{\max}} \\ l_{\max_i} = l_{r_i}(\overline{\alpha_{\max}}) \end{cases} \tag{29}$$

In the next section, the feasible design space for the springs is derived using the aforementioned conditions and mechanical feasibility.

4.2. *Design space for the springs of i^{th} R-joint*

The design of springs for the R-joint is conducted like that of the X-joint in Section 3.2. For the R-joint, in Eq. (8), expression of one third the joint width $(b/3)$ must be replaced by $(2r/3)$, and the conditions χ_{6a} and χ_{6b} must be adopted to cases A and B, discussed in the previous section. Also, the respective expressions for $l_{\max_i}$ derived in each of these cases should be used in the inequalities χ_1 and χ_4. Finally, the set of all conditions for spring design in the case of R-joint is obtained to be:

$$\boldsymbol{\chi}_a = \begin{cases} \chi_1\,(l_{\max_i} \text{ in Eq. (28)}) \\ \chi_2 \\ \chi_3 \\ \chi_4\,(l_{\max_i} \text{ in Eq. (28)}) \\ \chi_5 \\ \chi_{6a} := l_{0_i} :=]l_{l_i}(\overline{\alpha_{\max}}), 2h[\end{cases} \qquad \boldsymbol{\chi}_b = \begin{cases} \chi_1\,(l_{\max_i} = l_{r_i}(\overline{\alpha_{\max}})) \\ \chi_2 \\ \chi_3 \\ \chi_4\,(l_{\max_i} = l_{r_i}(\overline{\alpha_{\max}})) \\ \chi_5 \\ \chi_{6b} := l_{0_i} \in]0, l_{l_i}(\overline{\alpha_{\max}})] \end{cases} \tag{30}$$

Similar to the X-joint, the set of all feasible springs for the R-joint is obtained from $\boldsymbol{\chi}_a \cup \boldsymbol{\chi}_b$.

4.3. *Cross-sections and masses of the bars of 2-R manipulator*

There are 14 bars in the 2-R manipulator as shown in Fig 10(a). They are all designed exactly like those in the 2-X manipulator in Section 3.3. The reaction forces at the ends of the bars due to the contacting bars, actuating cables, and springs are shown in Fig. 12. The expressions for forces in the bars are presented in Eqs. (31) and (32). Unlike in the case of 2-X manipulator, these coefficients involve only two varying angles (α_1, α_2) and three constant angles $(\beta_0, \beta_1, \beta_2)$ in the offsets and joints (shown in Fig. 10(a)).

The forces due to payload, cables, and springs have the same bounds as in Eq. (14). On the other hand, the force coefficients belong to just two categories (I, IV) for this manipulator as presented in Table 3, and their bounds can be calculated as detailed in Section 3.3 and Appendix A. Finally, the bounds of forces in the bars can be overestimated, and their cross-section radii and masses can be computed in the same manner as illustrated for the 2-X manipulator. In this process, the symmetry of the manipulator is maintained about the configuration $(\alpha_1, \alpha_2) = (0, 0)$, by choosing identical radii for the bars $(1, 2), (4, 6), (8, 9), (11, 12), (13, 14)$.

$$\begin{cases} F_{14} &= \Omega_{\text{p}}^{14} F_{\text{p}} \\ F_{13} &= \Omega_{\text{p}}^{13} F_{\text{p}} \\ F_{12} &= \Omega_{14}^{12} F_{14} + \Omega_{Fk_{r_2}}^{12}(F_{r_2} + k_2(l_{r_2} - l_{0_2})) \\ F_{11} &= \Omega_{14}^{11} F_{14} + \Omega_{Fk_{r_2}}^{11}(F_{r_2} + k_2(l_{r_2} - l_{0_2})) \\ F_{10} &= \Omega_{13}^{10} F_{13} + \Omega_{Fk_{l_2}}^{10}(F_{l_2} + k_2(l_{l_2} - l_{0_2})) \\ F_9 &= \Omega_{11}^{9} F_{11} + \Omega_{10}^{9} F_{10} \\ F_8 &= \Omega_{11}^{8} F_{11} + \Omega_{10}^{8} F_{10} \\ F_7 &= \Omega_9^7 F_9 + \Omega_{F_{l_2}}^7 F_{l_2} + \Omega_{F_{r_2}}^7 F_{r_2} + \Omega_{k_{r_2}}^7 k_2(l_{r_2} - l_{0_2}) \\ F_6 &= \Omega_9^6 F_9 + \Omega_{F_{l_2}}^6 F_{l_2} + \Omega_{Fk_{r_2}}^6 (F_{r_2} + k_2(l_{r_2} - l_{0_2})) \\ F_5 &= \Omega_8^5 F_8 + \Omega_7^5 F_7 + \Omega_{F_{l_2}}^5 F_{l_2} + \Omega_{F_{r_2}}^5 F_{r_2} + \Omega_{k_{l_2}}^5 k_2(l_{l_2} - l_{0_2}) \\ F_4 &= \Omega_8^4 F_8 + \Omega_7^4 F_7 + \Omega_{F_{l_2}}^4 F_{l_2} + \Omega_{F_{r_2}}^4 F_{r_2} + \Omega_{k_{l_2}}^4 k_2(l_{l_2} - l_{0_2}) \\ F_3 &= \Omega_6^3 F_6 + \Omega_5^3 F_5 + \Omega_{F_{r_2}}^3 F_{r_2} + \Omega_{Fk_{r_1}}^3 (F_{r_1} + k_1(l_{r_1} - l_{0_1})) \\ F_2 &= \Omega_6^2 F_6 + \Omega_5^2 F_5 + \Omega_{F_{r_2}}^2 F_{r_2} + \Omega_{Fk_{r_1}}^2 (F_{r_1} + k_1(l_{r_1} - l_{0_1})) \\ F_1 &= \Omega_4^1 F_4 + \Omega_{F_{l_2}}^1 F_{l_2} + \Omega_{Fk_{l_1}}^1 (F_{l_1} + k_1(l_{l_1} - l_{0_1})) \end{cases} \tag{31}$$

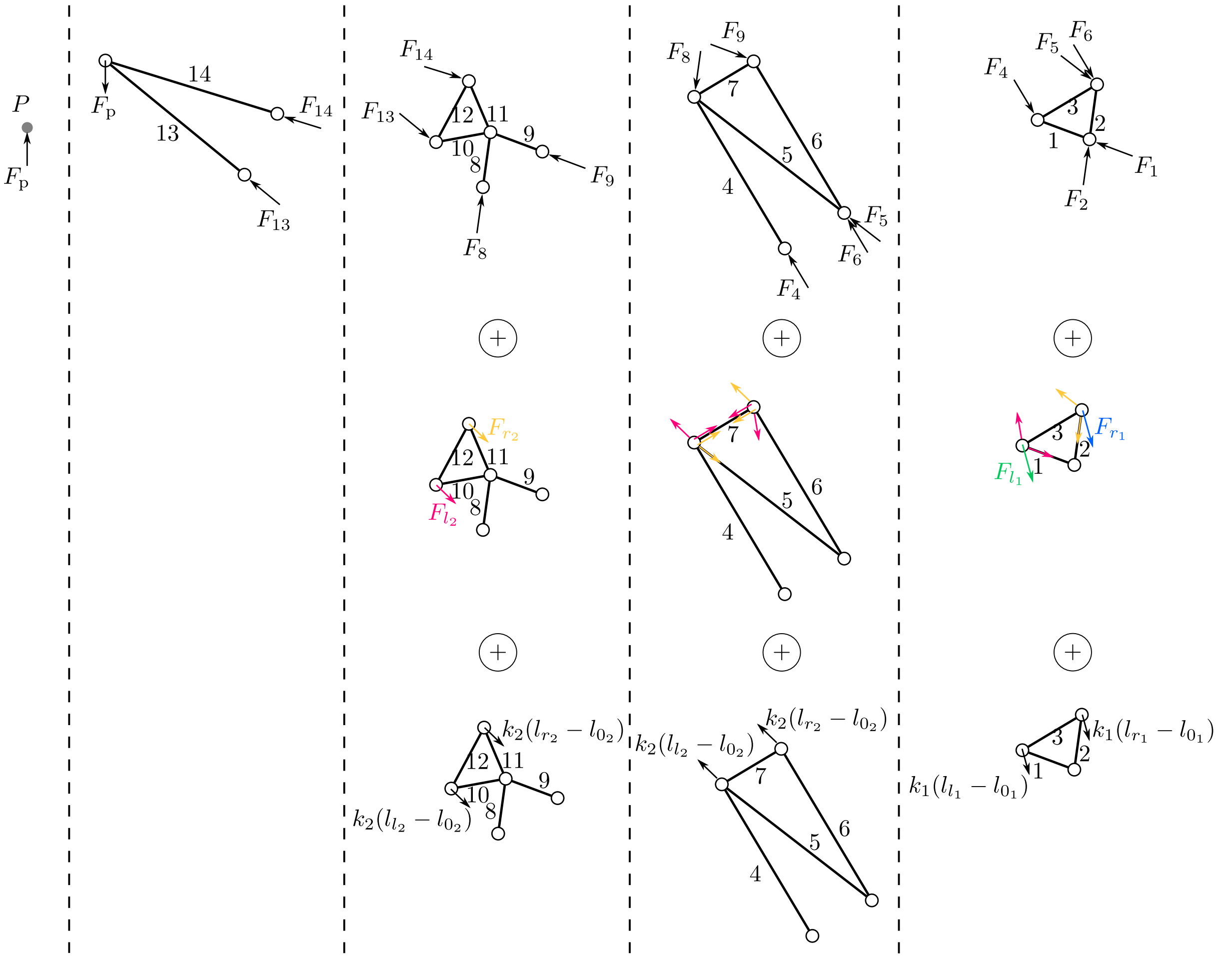

Figure 12: Reaction forces at the ends of the bars.

$$
\begin{cases}
\Omega_{\mathrm{p}}^{14} & = \csc(2\beta_2)\cos(\beta_2+\alpha_1+\alpha_2);\ \Omega_{\mathrm{p}}^{13} = \csc(2\beta_2)\cos(\beta_2-\alpha_1-\alpha_2); \\
\Omega_{14}^{12} & = -\sec(\beta_0)\cos(\beta_0-\beta_2);\ \Omega_{Fk_{r_2}}^{12} = -\sec(\beta_2)\sin(\beta_0-(\alpha_2/2)); \\
\Omega_{14}^{11} & = \sec(\beta_0)\sec(\beta_2);\ \Omega_{Fk_{r_2}}^{11} = \sec(\beta_0)\cos(\alpha_2/2); \\
\Omega_{13}^{10} & = \sec(\beta_0)\sin(\beta_2);\ \Omega_{Fk_{l_2}}^{10} = \sec(\beta_0)\cos(\alpha_2/2); \\
\Omega_{11}^{9} & = \csc(2\beta_0)\sin(\alpha_2);\ \Omega_{10}^{9} = \csc(2\beta_0)\sin(2\beta_0+\alpha_2); \\
\Omega_{11}^{8} & = \csc(2\beta_0)\sin(2\beta_0-\alpha_2);\ \Omega_{10}^{8} = -\csc(2\beta_0)\sin(\alpha_2); \\
\Omega_{9}^{7} & = -\sin(\beta_0); \Omega_{F_{l_2}}^{7} = 1+\cos(\beta_1);\ \Omega_{F_{r_2}}^{7} = 1+\sin(\alpha_2/2); \Omega_{k_{r_2}}^{7} = \sin(\alpha_2/2); \\
\Omega_{9}^{6} & = \cos(\beta_0);\ \Omega_{F_{l_2}}^{6} = \sin(\beta_1);\ \Omega_{Fk_{r_2}}^{6} = -\cos(\alpha_2/2); \\
\Omega_{8}^{5} & = -\sec(\beta_1)\sin(\beta_0);\ \Omega_{7}^{5} = -\sec(\beta_1);\ \Omega_{F_{l_2}}^{5} = -\sec(\beta_1)\left(-1+\sin(\alpha_2/2)\right); \\
\Omega_{F_{r_2}}^{5} & = 1+\sec(\beta_1);\ \Omega_{k_{l_2}}^{5} = -\sec(\beta_1)\sin(\alpha_2/2); \\
\Omega_{8}^{4} & = \cos(\beta_0)+\sin(\beta_0)\tan(\beta_1);\ \Omega_{7}^{4} = \tan(\beta_1); \\
\Omega_{F_{l_2}}^{4} & = -\cos(\beta_1+(\alpha_2/2))\sec(\beta_1)-\tan(\beta_1); \\
\Omega_{F_{r_2}}^{4} & = -\tan(\beta_1); \Omega_{k_{l_2}}^{4} = -\sec(\beta_1)\cos(\beta_1+(\alpha_2/2)); \\
\Omega_{6}^{3} & = -\tan(\beta_0);\ \Omega_{5}^{3} = -\cos(\beta_1)-\sin(\beta_1)\tan(\beta_0);\ \Omega_{F_{r_2}}^{3} = \sec(\beta_0)\cos(\beta_0-\beta_1); \\
\Omega_{Fk_{r_1}}^{3} & = -\sec(\beta_0)\sin(\beta_0-\alpha_1/2); \\
\Omega_{6}^{2} & = -\sec(\beta_0);\ \Omega_{5}^{2} = \sec(\beta_0)\sin(\beta_1);\ \Omega_{F_{r_2}}^{2} = 1-\sec(\beta_0)\sin(\beta_1); \\
\Omega_{Fk_{r_1}}^{2} & = \sec(\beta_0)\cos(\alpha_1/2); \\
\Omega_{4}^{1} & = \sec(\beta_0);\ \Omega_{F_{l_2}}^{1} = 1-\sec(\beta_0)\sin(\beta_1);\ \Omega_{Fk_{l_1}}^{1} = \sec(\beta_0)\cos(\alpha_1/2);
\end{cases}
\tag{32}
$$

Table 3: Classification of the coefficients in Eq. (32) and computation of their bounds.

Category	**Nature**	**Coefficients**	**Minimum**	**Maximum**
I	Constant	$\Omega^{12}_{14}, \Omega^{11}_{14}, \Omega^{10}_{13}, \Omega^{7}_{9}, \Omega^{7}_{F_{l_2}}$, $\Omega^{6}_{9}, \Omega^{6}_{F_{l_2}}, \Omega^{5}_{8}, \Omega^{5}_{7}, \Omega^{5}_{F_{r_2}}$, $\Omega^{4}_{8}, \Omega^{4}_{7}, \Omega^{4}_{F_{r_2}}, \Omega^{3}_{6}, \Omega^{3}_{5}$, $\Omega^{3}_{F_{r_2}}, \Omega^{2}_{6}, \Omega^{2}_{5}, \Omega^{2}_{F_{r_2}}, \Omega^{1}_{4}, \Omega^{1}_{F_{l_2}}$	Value of the constant	
IV	Possible extrema	$\Omega^{14}_{\mathrm{p}}, \Omega^{13}_{\mathrm{p}}, \Omega^{12}_{Fk_{r_2}}, \Omega^{10}_{Fk_{l_2}}$, $\Omega^{9}_{11}, \Omega^{9}_{10}, \Omega^{8}_{11}, \Omega^{8}_{10}, \Omega^{7}_{F_{r_2}}$, $\Omega^{7}_{k_{r_2}}, \Omega^{6}_{Fk_{r_2}}, \Omega^{5}_{F_{l_2}}, \Omega^{5}_{k_{l_2}}, \Omega^{4}_{F_{l_2}}$, $\Omega^{4}_{k_{l_2}}, \Omega^{3}_{Fk_{r_1}}, \Omega^{2}_{Fk_{r_1}}, \Omega^{1}_{Fk_{l_1}}$	Evaluate at stationary points, bounds; choose the minimum and maximum from them.	

4.4. *Static model of 2-R manipulator*

Following the same method as detailed in Section 3.4, the static equilibrium equations for the 2-R manipulator are also obtained in the form $(G_i = \Gamma_i), i = 1, 2$, where:

$$\begin{cases} G_1 = C_{1\mathrm{r}} \sin\alpha_1 + C'_{1\mathrm{r}} \sin(\alpha_1/2) - C_{3\mathrm{r}} \sin(\alpha_1 + \alpha_2) \\ G_2 = C_{2\mathrm{r}} \sin\alpha_1 + C'_{2\mathrm{r}} \sin(\alpha_2/2) - C_{3\mathrm{r}} \sin(\alpha_1 + \alpha_2) \\ \Gamma_1 = F_{l_1} \left(r\cos(\alpha_1/2) + h\sin(\alpha_1/2)\right) - F_{r_1} \left(r\cos(\alpha_1/2) - h\sin(\alpha_1/2)\right) \\ \Gamma_2 = F_{l_2} \left(r\cos(\alpha_2/2) + h\sin(\alpha_2/2)\right) - F_{r_2} \left(r\cos(\alpha_2/2) - h\sin(\alpha_2/2)\right) \end{cases} \tag{33}$$

with

$$\begin{cases} C_{1\mathrm{r}} = & -\frac{1}{2}ag(4m_{10} + 2m_{12} + 4m_{13} + 2m_4 + m_5 + 2m_7 + 4m_8 + 4m_{k_2} + 2m_{\mathrm{p}}) \\ & -gh(m_1 + 4m_{10} + 2m_{12} + 4m_{13} + m_3 + 2m_4 + m_5 + m_7 + 3m_8 + m_{k_1} + 3m_{k_2} + 2m_{\mathrm{p}}) \\ & +2k_1\left(r^2 - h^2\right) \\ C'_{1\mathrm{r}} = & 2hk_1 l_{0_1} \\ C_{2\mathrm{r}} = & 2k_2\left(r^2 - h^2\right) \\ C'_{2\mathrm{r}} = & 2hk_2 l_{0_2} \\ C_{3\mathrm{r}} = & g(a(m_{13} + m_{\mathrm{p}}) + h(m_{10} + m_{12} + 2m_{13} + m_{k_2} + m_{\mathrm{p}})) \end{cases} \tag{34}$$

The masses $(m_2, m_6, m_9, m_{11}, m_{14})$ have been replaced by $(m_1, m_4, m_8, m_{10}, m_{13})$ due to symmetry (see Fig. 10(a) and Section 4.3) of the manipulator. Similar to the 2-X manipulator, it can be shown that the coefficient of F_{l_i} (resp. F_{r_i}) is positive (resp. negative) in Eq. (33). Thus, the condition of equilibrium (α_1, α_2) can be satisfied only when $G_i \in \left[\underline{\Gamma_i}, \overline{\Gamma_i}\right]$ for $i = 1, 2$.

The stiffness matrix can be computed for the 2-R manipulator similarly as illustrated for the 2-X manipulator in Section 3.4. Upon eliminating the forces (F_{l_1}, F_{l_2}) from the equilibrium equations, one obtains the stiffness matrix in terms of the redundant forces as:

$$\mathbf{K}^{\mathrm{rr}}_{\alpha} = \begin{pmatrix} K^{\mathrm{rr}}_{11} & K_{12} \\ K_{12} & K^{\mathrm{rr}}_{22} \end{pmatrix} \text{ with } K^{\mathrm{rr}}_{11} = \frac{K^{\mathrm{rr}'}_{11}}{2\left(rc_1 + hs_1\right)} \text{ and } K^{\mathrm{rr}}_{22} = \frac{K^{\mathrm{rr}'}_{22}}{2\left(rc_2 + hs_2\right)} \tag{35}$$

where

$$\begin{cases} K^{\mathrm{rr}'}_{11} = 2C_{1\mathrm{r}}\left(c_1^3 r - hs_1^3\right) + C_{3\mathrm{r}}\{h(c_1 s_{12} - 2c_{12}s_1) + r(-2c_1c_{12} - s_1 s_{12})\} + C'_{1\mathrm{r}}r - 2hrF_{r_1} \\ K^{\mathrm{rr}'}_{22} = C_{3\mathrm{r}}\{h(c_2 s_{12} - 2c_{12}s_2) + r(-2c_{12}c_2 - s_{12}s_2)\} + C_{2\mathrm{r}}\left(2c_2^3 r - 2hs_2^3\right) + C'_{2\mathrm{r}}r - 2hrF_{r_2} \\ K_{12} = -C_{3\mathrm{r}}c_{12} \end{cases} \tag{36}$$

in which $c_1 = \cos(\alpha_1/2), s_1 = \sin(\alpha_1/2), c_2 = \cos(\alpha_2/2), s_2 = \sin(\alpha_2/2), c_{12} = \cos(\alpha_1 + \alpha_2), s_{12} = \sin(\alpha_1 + \alpha_2)$. The coefficient of F_{r_i} in the stiffness matrix is found to be $\frac{-2hr}{2(rc_i + hs_i)}$, for $i = 1, 2$. It can be shown that this coefficient is negative for all values of (r, h) when α_i is within limits due to cable actuation, i.e., $\in \left]-\overline{\overline{\alpha_{\max}}}, \overline{\overline{\alpha_{\max}}}\right[$ as defined in Eq. (26). This indicates that unlike in the 2-X manipulator, the stiffness decreases with the increase in actuation forces for the 2-R manipulator. This result is consistent with the one obtained for a single R-joint in [18]. In this case, the matrix corresponding to maximum stiffness must be obtained by setting two actuation forces to their minimum bound of $F_{\min}$. For instance, from Eq. (35),(36), one obtains $\overline{\mathbf{K}}^{\mathrm{rr}}_{\alpha} = \mathbf{K}^{\mathrm{rr}}_{\alpha}(F_{r_1} = F_{\min}, F_{r_2} = F_{\min})$. Similarly, the other stiffness matrices $\left(\overline{\mathbf{K}}^{\mathrm{rl}}_{\alpha}, \overline{\mathbf{K}}^{\mathrm{lr}}_{\alpha}, \overline{\mathbf{K}}^{\mathrm{ll}}_{\alpha}\right)$ can also be obtained by setting the redundant forces to $F_{\min}$.

As in the case of the 2-X manipulator, the SWFJ for this manipulator is formed by all (α_1, α_2) configurations where the conditions of wrench-feasibility and stability are satisfied. Their mapping onto the task space is conducted using the kinematic model defined in the next section.

4.5. Kinematic model of 2-R manipulator

From Fig. 1(b), the direct kinematics of 2-R manipulator can be expressed as:

$$\begin{cases} x = -(2h+a)\sin(\alpha_1) - (h+a)\sin(\alpha_1+\alpha_2) \\ y = h + (2h+a)\cos(\alpha_1) + (h+a)\cos(\alpha_1+\alpha_2) \end{cases} \tag{37}$$

Note that the kinematic model is independent of r.

It is well-known that the singularity of the 2-R manipulator occurs when $\alpha_2 = 0$ (fully stretched configuration) and $\alpha_2 = \pm\pi$ (folded back configuration). Recalling the joint limits $\alpha_i \in \left]-\frac{\pi}{2}, \frac{\pi}{2}\right[$, only the condition $\alpha_2 = 0$ is relevant for constructing the SWFW for this manipulator.

4.6. Stable wrench-feasible workspace of 2-R manipulator with a numerical example

The computation of SWFW for the 2-R manipulator follows the method described in Section 3.6. Notably, the discretization of α_1 and α_2 is performed within the joint limits of R-joint derived in Section 4.1.

Table 4: 2-R manipulator: Range of estimated buckling loads and the resulting safe cross-section radii for the bars along with their masses.

Bar index j	**Estimated load** [N]	**Cross-section radius** [mm] Computed ($r^*_{b_j}$)	**Cross-section radius** [mm] Corrected (r_{b_j})	**Mass** [kg] m_j
14	[-30.62, 65.65]	2.37	5.00	0.1081
13	[-30.62, 65.65]	2.37		
12	[-282.37, 23.34]	1.15	5.00	0.0424
11	[-34.67, 445.61]	2.39	5.00	0.0424
10	[-34.67, 445.61]	2.39		
9	[-193.60, 656.81]	2.64	5.00	0.0424
8	[-193.60, 656.81]	2.64		
7	[-346.87, 619.92]	2.60	5.00	0.0424
5	[-2603.15, 2603.15]	6.11	6.11	0.1704
6	[-489.19, 754.51]	4.32	6.07	0.1561
4	[-2716.72, 2939.62]	6.07		
3	[-3065.23, 2826.14]	3.80	5.00	0.0424
2	[-3370.15, 4120.78]	4.17	5.00	0.0424
1	[-3151.42, 3853.07]	4.11		
			Total bar mass	1.0805
			Mass of springs ($2(m_{k_1} + m_{k_2})$)	4.4639
			Total moving mass of the manipulator	5.5444

As a numerical illustration, the following design is considered: $r = 0.1$ m, $h = 0.1732$ m, $a = 0.5$ m. These parameters ensure that the height and width for the joints and offsets of the 2-R manipulator are the same as those of the 2-X manipulator considered in Section 3.7. The other design parameters are assumed to be: $\sigma_\alpha = (9/10)$, $k_1 = 5000$ N/m, $\sigma_{k_1} = 0.7$, $k_2 = 2000$ N/m, $\sigma_{k_2} = 0.5$, $F_{\max} = 200$ N. The springs chosen are much stiffer than in the case of the 2-X manipulator, as those springs could not stabilize the 2-R manipulator at $(\alpha_1, \alpha_2) = (0, 0)$, in the absence of actuation forces. The main steps involved in computing the SWFJ and SWFW are listed in the following:

- **Section 4.2**: The computation of feasible design space for the springs of R-joint was performed in the same manner as illustrated for the X-joint in Section 3.7. The dependent parameters of spring 1 ($k_1 = 5000$ N/m$, \sigma_{k_1} = 0.7$), are: $d = 5.7$ mm, $D = 36.2069$ mm, $N_a = 45.3131$, $l_{0_1} = 0.3250$ m, $l_{\max_1} = 0.3644$ m, $m_{k_1} = 1.1008$ kg. The dependent parameters of spring 2 ($k_2 = 3000$ N/m$, \sigma_{k_2} = 0.5$) are: $d = 5.3$ mm, $D = 45.4872$ mm, $N_a = 42.7045$, $l_{0_2} = 0.3120$ m, $l_{\max_1} = 0.3728$ m, $m_{k_2} = 1.1311$ kg.
- **Section 4.1**: While $\sigma_\alpha = (9/10)$, $\overline{\alpha_{\max}} = 0.9425$ rad. From the free length of the springs, the actual maximum limit of movement for the two joints are found to be $\alpha_{\max_1} = 0.1976$ rad, $\alpha_{\max_2} = 0.3050$ rad, respectively, which shows that both springs belong to the set χ_a in the spring design space (i.e., case A in Fig. 4(a)).
- **Section 4.3**: The bounds estimated for the axial forces in the bars, their cross-section radii, and masses are presented in Table 4. The total moving mass is computed to be 5.5444 kg, with maximum contribution from the springs.
- **Sections 4.4, 4.5, 4.6**: Using the static and kinematic models of the manipulator, its SWFJ and SWFW are constructed as shown in Figs. 13(a) and 13(b), respectively. The opaque and transparent styles for the boundaries have the same meaning as described for the 2-X manipulator in Section 3.7.

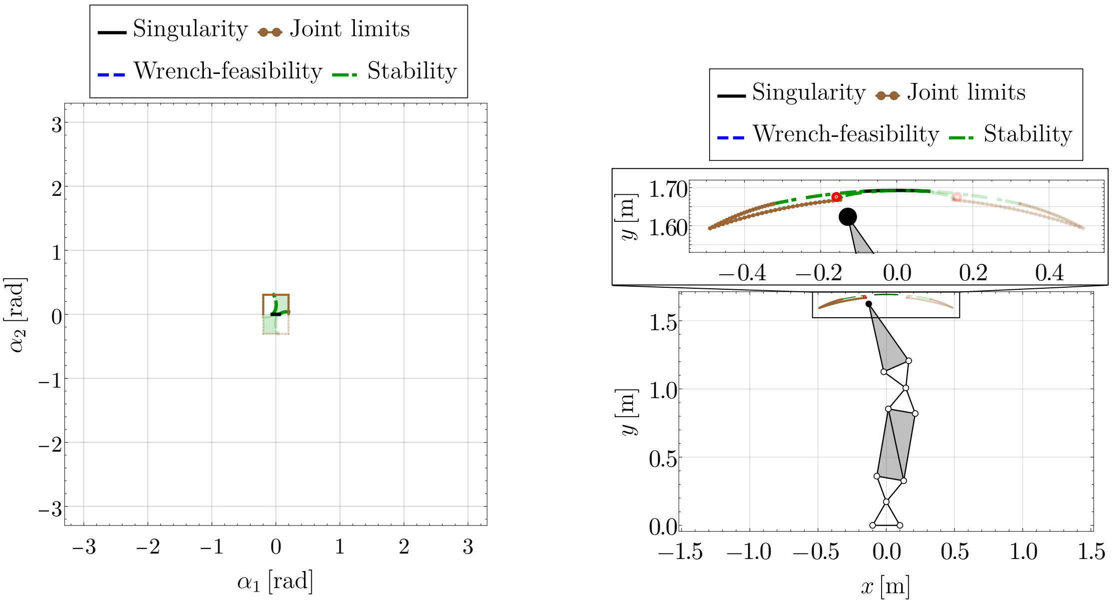

(a) SWFJ highlighted in shading

(b) SWFW with two maximal inscribed disks (of radius 0.0086 m each)

Figure 13: The stable wrench-feasible joint space (SWFJ) and stable wrench-feasible workspace (SWFW) for the 2-R manipulator with: $r = 0.1$ m, $h = 0.1732$ m, $a = 0.5$ m, $\sigma_\alpha = (9/10)$, $k_1 = 5000$ N/m, $l_{0_1} = 0.3250$ m, $m_{k_1} = 1.1008$ kg, $k_2 = 2000$ N/m, $l_{0_2} = 0.3120$ m, $m_{k_2} = 1.1311$ kg, $F_{\max} = 200$ N/m. In the joint space (α_1, α_2), the curves lying in the region $(\alpha_2 > 0)$ are shown in opaque style while those in the region $(\alpha_2 < 0)$ are shown in transparent style. The images of these curves in the task space are also shown in the same style for the sake of clarity.

From Fig. 13(a), it is observed that the joint limits are much stronger for the 2-R manipulator when compared to its counterpart in Fig. 9(a). This is mainly due to the geometry of the R-joint and the actuation scheme with cables, which limit the maximum amplitude of joint movement to $\frac{\pi}{2}$ (see Eq. (26)). Consequently, the 2-R manipulator has a much smaller SWFJ and SWFW than the 2-X manipulator. Therefore, the two maximally inscribed disks (radius = 0.0086 m) are much smaller than the ones found for the 2-X manipulator (radius = 0.0736 m) in Fig. 9(b). The maximum vertical reach of the manipulator is nearly 200 times the radius of the maximal inscribed disk. Thus, the design is a very poor one. For this design, it takes about 7 ms (averaged over 100 runs) to compute the SWFW, which is over five times faster than that of the 2-X manipulator.

From Fig. 13, it is also observed that the stability boundary is very close to the home configuration $(\alpha_1, \alpha_2) = (0, 0)$, indicating that it is difficult to stabilize the 2-R manipulator, even with springs of large stiffness, unlike its counterpart.

5. Conclusions

Two planar cable-driven tensegrity-inspired manipulators composed of two anti-parallelogram (X) joints and two revolute (R) joints, respectively, were studied in this work. These joints are remotely actuated with two cables, each, by motors attached to the base. The joints also have springs on the two sides to stabilize the manipulator while it carries a payload at the end-effector in the presence of gravity. Globally, a method to compute the stable wrench-feasible workspace of these manipulators, which accounts for the mechanical feasibility of its constituent elements, was presented.

A systematic study of the joint limits due to the geometry and cable actuation was presented. The conditions responsible for the mechanical feasibility of the springs, namely, allowable shear stress, recommended spring index, standard wire diameters, minimum number of active coils, and safe helix angle, were used to construct the feasible design space for the springs. Two parameters are needed to access all the springs inside this space. The interdependence of the actual joint limits and the free length of the springs were explored on a case-by-case basis, covering all the possibilities exhaustively.

A method for finding safe cross-sections of the bars in these manipulators was proposed. Since all the bars in tensegrity-inspired manipulators are only loaded axially, a geometric approach has been used to compute the axial forces in the bars due to the payload, cable actuation, and springs. Using the limits on the movement of each joint and the range of forces achievable with the cables and springs, upper limits for compressive loads in the bars were obtained. These limits were used to determine safe cross-sections for the bars. Further, it was ensured that the mass symmetry of the manipulators is preserved and the sections are large enough to avoid fabrication difficulties.

Subsequently, the kinematic and static models of the manipulators were formulated. It was found that the 2-X manipulator (resp. 2-R manipulator) has a positive (resp. negative) correlation between actuation forces and stiffness. By imposing realistic bounds on the cable forces, their stable wrench-feasible joint spaces (SWFJ) and stable wrench-feasible workspaces (SWFW) were computed. In order to quantify the size of SWFW, maximal disk(s) was inscribed inside it, and its radius was evaluated.

Numerical examples of 2-X and 2-R manipulators were presented, such that they have similar bar lengths and cable forces.

The springs were chosen to ensure stability at the vertically straight configuration for both manipulators in the absence of actuation forces. While the two manipulators have a comparable moving mass, the size of the SWFW for the 2-X manipulator is nearly 10 times larger (as evaluated by the radius of the inscribed disk) than that of the 2-R manipulator. However, for both manipulators, the radius of the inscribed disk in SWFW itself is much smaller (0.005-0.05 times) compared to their maximum vertical reach. Due to a higher complexity of the model of the 2-X manipulator, the time taken to compute its SWFW with the inscribed disk (43 ms) is about six times that of the 2-R manipulator (7 ms). Nevertheless, the time taken is of the order of milliseconds for both manipulators, making the proposed computation scheme suitable for exploring several designs in an optimization framework.

It is noted that the observations reported on workspace sizing are specific to the examples in this paper and do not extend to all the designs of these manipulators. A more conclusive study must find *good* designs for the two tensegrity-inspired manipulators and study their properties. This problem will be addressed in the future through design optimization of the 2-X and 2-R manipulators for the same inscribed disk in SWFW.

The overall design process illustrated for the two manipulators is generic and is, in principle, applicable to other architectures of planar tensegrity-inspired manipulators. It can also be adapted to different actuation schemes of the cables and different placements of the manipulator (e.g., ceiling-mounted systems like the Delta robot) by appropriately adjusting the direction of gravity.

Appendix A. Illustrations on the categorization of the force coefficients in the design of bars of 2-X manipulator

This section illustrates the algebraic steps involved in categorizing the force coefficients in Table 1 with one example each. The coefficients in category I need no processing. Hence, one coefficient from the remaining categories is chosen and studied in the following:

- **Category II**: From Eq. (13), $\Omega_{11}^{10} = \csc(\psi_2 - \alpha_2)\sin(\beta_2 + \alpha_2 - \psi_2)$. Substituting for ψ_2 in terms of α_2 using the loop-closure equation (see [31]) and recalling that $\alpha_2 = 2\theta_2$, the above coefficient can be rewritten solely in terms of θ_2 as:

$$\Omega_{11}^{10} = -\frac{\sec\theta_2 \cos(\beta_2 + \theta_2)\sqrt{\lambda^2 - \cos^2\theta_2} + \sin(\beta_2 + \theta 2)}{\sqrt{\lambda^2 - \cos^2\theta_2} + \sin\theta_2} \tag{A.1}$$

  where $\lambda = (l/b)$. Differentiation w.r.t. θ_2 results in:

$$\frac{\mathrm{d}\Omega_{11}^{10}}{\mathrm{d}\theta_2} = \frac{\lambda^2 \sin(\beta_2)\sec^2\theta_2}{\sqrt{\lambda^2 - \cos^2\theta_2}(\sqrt{\lambda^2 - \cos^2\theta_2} + \sin\theta_2)} \tag{A.2}$$

  Recalling that $\lambda > 1$ (see Section 2), it can be shown that the denominator is strictly positive when $\theta_2 \in \left[-\frac{\pi}{2}, \frac{\pi}{2}\right]$ (see [18]). Additionally, since $\beta_2 \in \left[0, \frac{\pi}{2}\right]$ (see Fig. 2(a)), it follows that $\frac{\mathrm{d}\Omega_{11}^{10}}{\mathrm{d}\theta_2} > 0$. Thus, Ω_{11}^{10} increases monotonically with $\theta_2 \in [-\frac{\pi}{2}, \frac{\pi}{2}]$, or, equivalently with $\alpha_2 \in [-\pi, \pi]$.

- **Category III**: From Eq. (13), $\Omega_{Fk_{l_2}}^{9} = \csc(\psi_2 - \alpha_2)\cos(\theta_2 - \psi_2)$. As in the previous case, the force coefficient and its first derivative can be written as:

$$\Omega_{Fk_{l_2}}^{9} = \frac{\lambda}{\sqrt{\lambda^2 - \cos^2\theta_2} + \sin\theta_2} \tag{A.3}$$

$$\frac{\mathrm{d}\Omega_{Fk_{l_2}}^{9}}{\mathrm{d}\theta_2} = -\frac{\lambda\cos\theta_2}{\sqrt{\lambda^2 - \cos^2\theta_2}(\sqrt{\lambda^2 - \cos^2\theta_2} + \sin\theta_2)} \tag{A.4}$$

  Clearly, $\frac{\mathrm{d}\Omega_{Fk_{l_2}}^{9}}{\mathrm{d}\theta_2} < 0$ while $\theta_2 \in [-\frac{\pi}{2}, \frac{\pi}{2}]$, or $\alpha_2 \in [-\pi, \pi]$. This implies that $\Omega_{Fk_{l_2}}^{9}$ monotonically decreases in the specified domain.

- **Category IV**: From Eq. (13), $\Omega_{11}^{9} = \csc(\psi_2 - \alpha_2)\sin(\beta_2)$. It can be rewritten as:

$$\Omega_{11}^{9} = \frac{\lambda\sec\theta_2\sin\beta_2}{\sqrt{\lambda^2 - \cos^2\theta_2} + \sin\theta_2} \tag{A.5}$$

  Differentiating w.r.t. θ_2 yields:

$$\frac{\mathrm{d}\Omega_{11}^{9}}{\mathrm{d}\theta_2} = \frac{\lambda\sin\beta_2(\sqrt{\lambda^2 - \cos^2\theta_2}\tan\theta_2\sec\theta_2 - 1)}{\sqrt{\lambda^2 - \cos^2\theta_2}(\sin\theta_2 + \sqrt{\lambda^2 - \cos^2\theta_2})} \tag{A.6}$$

  Unlike in the previous cases, the above expression is not provably positive or negative. Hence, there is a possible extrema for Ω_{11}^{9} within the domain of interest. The associated stationary points can be found from the zeros of the function in

Eq. (A.6). Since the denominator and the first two factors in the numerator are positive, only the remaining factor must be considered for finding the zeros. This results in:

$$\sqrt{\lambda^2-\cos^2\theta_2}\tan\theta_2\sec\theta_2-1=0 \tag{A.7}$$

$$\implies \sqrt{\lambda^2-\cos^2\theta_2}=\frac{1}{\tan\theta_2\sec\theta_2} \tag{A.8}$$

Squaring both sides and incorporating the tangent half-angle substitutions: $\sin\theta_2=\frac{2t_2}{1+t_2^2}$ and $\cos\theta_2=\frac{1-t_2^2}{1+t_2^2}$, with $t_2=\tan\left(\frac{\theta_2}{2}\right)$, one obtains:

$$\frac{\left(1+t_2^2\right)^2\left(t_2^4-2\left(2\lambda^2+1\right)t_2^2+1\right)}{\left(1+t_2^2\right)^2}=0 \tag{A.9}$$

Clearing the non-zero factors in the numerator and denominator yields:

$$t_2^4-2\left(2\lambda^2+1\right)t_2^2+1=0 \tag{A.10}$$

The zeros of this polynomial contain the stationary points (if any) and possibly some spurious solutions to $\frac{\mathrm{d}\Omega_{11}^9}{\mathrm{d}\theta_2}=0$ (introduced due to squaring of Eq. (A.8)). Note that these roots depend only on the ratio $\lambda=(l/b)$, and only the real roots within the bounds of θ_2 (equivalent to those of α_2) are of interest. The function Ω_{11}^9 can be evaluated at these roots as well as the bounds of θ_2 to form a set. Then, the lower and upper bounds of Ω_{11}^9 can be found as the minimum and maximum values, respectively, in this set.

Appendix B. Computation of actual compressive loads in the bars and validation of 2-X and 2-R designs

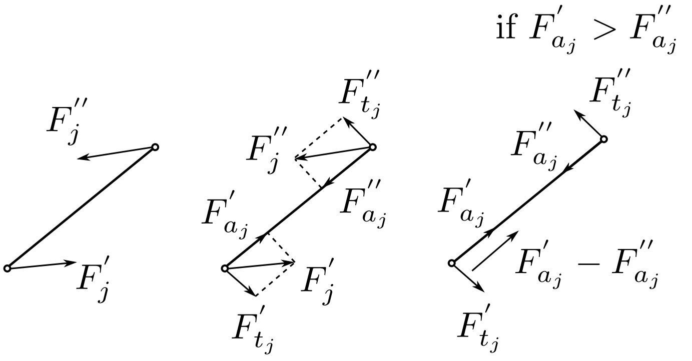

Figure B.14: Computation of the buckling load in the bar j subjected to forces F'_j and F''_j at the two ends.

This section aims to show that the critical values for buckling load assumed in the design process (see Tables 2 and 4) are larger than the actual loads experienced by the bars in 2-X and 2-R manipulators.

This study is conducted inside the SWFJ at equilibrium configurations for both manipulators. Since four cables redundantly actuate these manipulators, it is necessary to specify the two redundant forces along with the configuration while defining their static models. As a first step, the Newton-Euler equations were developed for each of the bars in the two manipulators. The masses of the bars, as well as the springs (see Sections 3.7 and 4.6), are included in this model to determine the reaction forces accurately.

Then, the joint space (α_1,α_2) is discretized into 900 equally spaced grid points within the joint limits. Of these, the points inside the SWFJ are selected as feasible configurations. At each point, 100 combinations of redundant forces $\in[F_{\min},F_{\max}]$ are considered to cover the actuation force space sufficiently. Finally, the static model is solved at the chosen configuration for the assumed combination of redundant forces to determine the reaction forces at the ends of the bars.

For a bar j, the forces acting at the two ends are shown in Fig. B.14(left). Note that these forces are not directed along the axis of the bar as assumed in the design process (see Sections 3.3 and 4.3). This is to balance the forces and moments induced by the self-weight of the bar, which were neglected during the design process.

Next, the reaction forces at the two ends of the bar are resolved into the axial and transverse directions, as shown in Fig. B.14(center). Since only the axial component of reactions is responsible for buckling, only F'_{a_j} and F''_{a_j} are considered in further computations. When both these forces point in the same direction, no axial stresses are induced in the bar. When their directions are opposite but directed away from the center of the bars, then they induce tensile stresses in the bar, which cannot cause buckling failure. However, when the forces are directed toward the center of the bar, buckling is possible. The difference in the magnitude of these forces balances the self-weight component, while $\min(F^{'}_{a_j}, F^{''}_{aj})$ induces a buckling load in the bar. Hence, the numerical value of $\min\left(F^{'}_{a_j}, F^{''}_{a_j}\right)$ is quantified as the actual buckling load faced by this bar (see Fig. B.14(right)).

The above computation is performed for all the bars at each grid point inside the SWFJ and the chosen levels of redundant forces. The minimum and maximum values of the axial loads for each of the bars are presented along with their assumed values in Table B.5 (resp. B.6) for the 2-X manipulator (resp. 2-R manipulator).

It is observed that the range of actual load lies within the range of estimated load for the bars in both manipulators. This validates the manipulator designs as safe and free from buckling failure.

Table B.5: Ranges of the estimated load and the actual load in the bars of the 2-X manipulator. The positive sign indicates compressive loading while the negative sign indicates tensile loading.

Bar index (j)	**Estimated load** [N]	**Actual load** [N]
12	[-101.92, 101.92]	[-53.50, 53.51]
11	[-101.92, 101.92]	[-53.50, 53.51]
10	[-461.71, 162.19]	[-174.79, -42.30]
9	[-173.81, 772.84]	[87.79, 361.38]
8	[-173.81, 772.84]	[87.79, 361.38]
7	[-726.05, 807.06]	[-57.25, 328.22]
6	[-567.46, 958.53]	[-72.66, 283.76]
5	[-4128.03, 4128.03]	[-218.52, 218.00]
4	[-4091.47, 4107.72]	[-158.60, 377.77]
3	[-8434.49, 8240.10]	[-311.62, 278.13]
2	[-9041.49, 10451.80]	[384.62, 831.61]
1	[-9694.20, 11896.80]	[384.62, 831.61]

Table B.6: Ranges of the estimated load and the actual load in the bars of the 2-R manipulator. The positive sign indicates compressive loading while the negative sign indicates tensile loading.

Bar index (j)	**Estimated load** [N]	**Actual load** [N]
14	[-30.62, 65.65]	[-15.73, 34.10]
13	[-30.62, 65.65]	[-15.73, 34.10]
12	[-282.37, 23.34]	[-166.97, -38.64]
11	[-34.67, 445.61]	[55.05, 369.02]
10	[-34.67, 445.61]	[55.05, 369.02]
9	[-193.60, 656.81]	[80.42, 361.92]
8	[-193.60, 656.81]	[80.42, 361.92]
7	[-346.87, 619.92]	[-49.71, 309.58]
6	[-489.19, 754.51]	[-15.55, 253.20]
5	[-2603.15, 2603.15]	[-51.87, 51.85]
4	[-2716.72, 2939.62]	[-43.63, 221.51]
3	[-3065.23, 2826.14]	[-195.39, 3.56]
2	[-3370.15, 4120.78]	[122.71, 635.37]
1	[-3151.42, 3853.07]	[122.71, 635.37]

References

[1] D. Riedelbauch, N. Höllerich, D. Henrich, Benchmarking teamwork of humans and cobots—an overview of metrics, strategies, and tasks, IEEE Access 11 (2023) 43648–43674. `doi:10.1109/ACCESS.2023.3271602`.

[2] A. Keshvarparast, D. Battini, O. Battaia, A. Pirayesh, Collaborative robots in manufacturing and assembly systems: literature review and future research agenda, Journal of Intelligent Manufacturing (2023). `doi:10.1007/s10845-023-02137-w`.

[3] F. Iida, A. J. Ijspeert, Biologically Inspired Robotics, Springer International Publishing, Cham, 2016, pp. 2015–2034. `doi:10.1007/978-3-319-32552-1_75`.

[4] S. Kim, C. Laschi, B. Trimmer, Soft robotics: a bioinspired evolution in robotics, Trends in Biotechnology 31 (5) (2013) 287–294. `doi:10.1016/j.tibtech.2013.03.002`.

[5] Y.-L. Park, B.-R. Chen, N. O. Pérez-Arancibia, D. Young, L. Stirling, R. J. Wood, E. C. Goldfield, R. Nagpal, Design and control of a bio-inspired soft wearable robotic device for ankle–foot rehabilitation, Bioinspiration & Biomimetics 9 (1) (2014) 016007. `doi:10.1088/1748-3182/9/1/016007`.

[6] M. Calisti, M. Giorelli, G. Levy, B. Mazzolai, B. Hochner, C. Laschi, P. Dario, An octopus-bioinspired solution to movement and manipulation for soft robots, Bioinspiration & Biomimetics 6 (3) (2011) 036002. `doi:10.1088/1748-3182/6/3/036002`.

[7] S. Lessard, D. Castro, W. Asper, S. D. Chopra, L. B. Baltaxe-Admony, M. Teodorescu, V. SunSpiral, A. Agogino, A bio-inspired tensegrity manipulator with multi-DOF, structurally compliant joints, in: 2016 IEEE/RSJ International Conference on Intelligent Robots and Systems (IROS), 2016, pp. 5515–5520. `doi:10.1109/IROS.2016.7759811`.

[8] S. Kolachalama, S. Lakshmanan, Continuum robots for manipulation applications: A survey, Journal of Robotics (2020) . `doi:10.1155/2020/4187048`.

[9] T. da Veiga, J. H. Chandler, P. Lloyd, G. Pittiglio, N. J. Wilkinson, A. K. Hoshiar, R. A. Harris, P. Valdastri, Challenges of continuum robots in clinical context: a review, Progress in Biomedical Engineering 2 (3) (2020) 032003. `doi:10.1088/2516-1091/ab9f41`.

[10] Z. Yang, H. Yang, Y. Cao, Y. Cui, L. Zhang, Magnetically actuated continuum medical robots: A review, Advanced Intelligent Systems (2023) 2200416 `doi:{10.1002/aisy.202200416}`.

[11] K. Sakai, T. Kikuchi, I. Abe, Development of bio-inspired knee joint for power assist suit, in: 2015 IEEE International Conference on Robotics and Biomimetics (ROBIO), 2015, pp. 523–528. `doi:10.1109/ROBIO.2015.7418821`.

[12] R. E. Skelton, M. de Oliveira, Tensegrity Systems, Springer, United States, 2009. `doi:10.1007/978-0-387-74242-7`.

[13] C. Sultan, Tensegrity: 60 years of art, science, and engineering, in: Advances in Applied Mechanics, Vol. 43 of Advances in Applied Mechanics, Elsevier, 2009, pp. 69–145. `doi:10.1016/S0065-2156(09)43002-3`.

[14] M. Arsenault, C. M. Gosselin, Kinematic, static and dynamic analysis of a planar 2-DOF tensegrity mechanism, Mechanism and Machine Theory 41 (9) (2006) 1072–1089. `doi:10.1016/j.mechmachtheory.2005.10.014`.

[15] C. D. Crane, J. Bayat, V. Vikas, R. Roberts, Kinematic analysis of a planar tensegrity mechanism with pre-stressed springs, in: J. Lenarčič, P. Wenger (Eds.), Advances in Robot Kinematics: Analysis and Design, Springer Netherlands, Dordrecht, 2008, pp. 419–427. `doi:10.1007/978-1-4020-8600-7_44`.

[16] J. Begey, M. Vedrines, N. Andreff, P. Renaud, Selection of actuation mode for tensegrity mechanisms: The case study of the actuated Snelson cross, Mechanism and Machine Theory 152 (2020) 103881. `doi:10.1016/j.mechmachtheory.2020.103881`.

[17] Q. Boehler, S. Abdelaziz, M. Vedrines, P. Poignet, P. Renaud, From modeling to control of a variable stiffness device based on a cable-driven tensegrity mechanism, Mechanism and Machine Theory 107 (2017) 1–12. `doi:10.1016/j.mechmachtheory.2016.09.015`.

[18] V. Muralidharan, P. Wenger, Optimal design and comparative study of two antagonistically actuated tensegrity joints, Mechanism and Machine Theory 159 (2021) 104249. `doi:10.1016/j.mechmachtheory.2021.104249`.

[19] V. Muralidharan, N. Testard, C. Chevallereau, A. Abourachid, P. Wenger, Variable stiffness and antagonist actuation for cable-driven manipulators inspired by the bird neck, Journal of Mechanisms and Robotics 15 (3) (2023). `doi:10.1115/1.4062302`.

[20] W. Guo, F. Gao, Solution space atlases, workspace characteristics charts and joint space maps for the design of planar serial manipulators, Mechanism and Machine Theory 45 (3) (2010) 392–407. `doi:10.1016/j.mechmachtheory.2009.09.012`.

[21] C. Yang, W. Ye, Q. Li, Review of the performance optimization of parallel manipulators, Mechanism and Machine Theory 170 (2022) 104725. `doi:10.1016/j.mechmachtheory.2022.104725`.

[22] Q. Boehler, I. Charpentier, M. S. Vedrines, P. Renaud, Definition and computation of tensegrity mechanism workspace, Journal of Mechanisms and Robotics 7 (4) (2015) 044502. `doi:10.1115/1.4029809`.

[23] M. Hägele, K. Nilsson, J. N. Pires, Industrial robotics, in: B. Siciliano, O. Khatib (Eds.), Springer Handbook of Robotics, Springer, Berlin, Heidelberg, 2008, pp. 963–986. `doi:10.1007/978-3-540-30301-5_43`.

[24] M. Furet, P. Wenger, Kinetostatic analysis and actuation strategy of a planar tensegrity 2-X manipulator, Journal of Mechanisms and Robotics 11 (6) (2019) 060904. `doi:10.1115/1.4044209`.

[25] S. K. Mustafa, S. K. Agrawal, On the force-closure analysis of n-dof cable-driven open chains based on reciprocal screw theory, IEEE Transactions on Robotics 28 (1) (2012) 22–31. `doi:10.1109/TRO.2011.2168170`.

[26] V. Muralidharan, P. Wenger, C. Chevallereau, Kinematic and static analysis of a cable-driven 2-X tensegrity manipulator for two actuation strategies, in: O. Altuzarra, A. Kecskeméthy (Eds.), Advances in Robot Kinematics 2022, Springer International Publishing, Cham, 2022, pp. 149–159.

[27] V. Muralidharan, Computation of the feasible design space for helical extension springs and its parametric representation, Technical Report, LS2N, École Centrale de Nantes (2022).

[28] P. R. N. Childs, Mechanical Design: Theory and Applications, 3rd Edition, Butterworth-Heinemann, 2021. `doi:10.1016/B978-0-12-821102-1.00015-9`.

[29] European Standard, EN 10270-1:2022 - Steel wire for mechanical springs - Part 1: Patented cold drawn unalloyed spring steel wire (2022).

[30] R. K. Bansal, A textbook of strength of materials, 4th Edition, Laxmi Publications, New Delhi, India, 2009.

[31] M. Furet, A. van Riesen, C. Chevallereau, P. Wenger, Optimal design of tensegrity mechanisms used in a bird neck model, in: B. Corves, P. Wenger, M. Hüsing (Eds.), EuCoMeS 2018, Vol. 59, Springer International Publishing, Cham, 2019, pp. 365–375. `doi:10.1007/978-3-319-98020-1_43`.

[32] V. Muralidharan, P. Wenger, C. Chevallereau, Computation of stable wrench-feasible workspace of cable driven n-X manipulator, in: Proceedings of the 25ème Congrès Français de Mécanique, Nantes, France, 2022.

[33] V. Muralidharan, Stable wrench-feasible workspace of a 2-X tensegrity manipulator, Technical report, LS2N, École Centrale de Nantes (2022).

[34] P. Wenger, M. Furet, Kinematic analysis of a planar manipulator with anti-parallelogram joints and offsets, in: J. Lenarčič, B. Siciliano (Eds.), Advances in Robot Kinematics 2020, Springer International Publishing, Cham, 2021, pp. 319–326.

[35] M. K. Karnam, A. Baskar, R. A. Srivatsan, S. Bandyopadhyay, Computation of the safe working zones of planar and spatial parallel manipulators, Robotica 38 (5) (2020) 861–885. `doi:10.1017/S0263574719001139`.

[36] X. Diao, O. Ma, Q. Lu, Singularity analysis of planar cable-driven parallel robots, in: 2008 IEEE Conference on Robotics, Automation and Mechatronics, 2008, pp. 272–277. `doi:10.1109/RAMECH.2008.4681507`.